Journal of Fluids and Structures 116 (2023) 103804

Contents lists available at ScienceDirect

Journal of Fluids and Structures

journal homepage: www.elsevier.com/locate/jfs

Hydroelastic response of concrete shells during impact on calm water

Bjørn C. Abrahamsen [a,*], Frode Grytten [b], Øyvind Hellan [a], Tore H. Søreide [c], Odd M. Faltinsen [d]

[a] SINTEF Ocean, Otto Nielsens veg 10, 7052 Trondheim, Norway
[b] SINTEF Industry, Dept. Materials and Nanotech., Pb. 124 Blindern, 0314 Oslo, Norway
[c] Independent researcher, Trondheim, Norway
[d] NTNU, Centre for Autonomous Marine Operations and Systems (AMOS), Otto Nielsens veg 10, 7052 Trondheim, Norway

ARTICLE INFO

Article history:
Received 14 March 2022
Received in revised form 17 November 2022
Accepted 18 November 2022
Available online 12 December 2022

Keywords:
Hydroelasticity
Concrete
Drop test
Finite element analysis
Water impact
Slamming

ABSTRACT

Many ocean structures located offshore are supported by large vertical concrete columns. High and steep storm waves – in the process of breaking – may induce large local slamming loads on these columns. The present work is related to the fundamental physics of the local hydroelastic shell response due to slamming.

The concrete columns supporting typical offshore structures are large. The size means that full scale tests of a segment of the column is impractical and expensive. Model-scale testing in a wave tank is also challenging. Firstly, the scaling of structural properties need to adhere to the scaling laws of hydrodynamics. Secondly, the manufacturing of realistic Froude scaled elastic shell models is hard since curved shells carries loads by a combination of bending and membrane action. The challenge is to scale both the bending and membrane action properly. One part of this study shows how realistic Froude scaled elastic shells representing concrete shells can be designed.

The second part of this study presents results from experimental and numerical analysis of drop tests. Numerical hydroelastic analyses of both the elastic model shells and the real concrete shells are presented. The results show that even large and thick concrete shells experience significant hydroelastic effects during slamming.

The hydroelastic response of the concrete shells is dominated by only a few structural eigenmodes. This means that the calculated dynamic amplification factors, DAF, resemble those of one-degree-of-freedom mass–spring systems exposed to loads of finite duration.

The structural responses are seen to significantly modify the hydrodynamic loads. This hydrodynamic load modification consists of the well-known added mass term but also a time dependent slam damping term which reduce the structural response when properly accounted for. Both terms are necessary to calculate the concrete shell response accurately.

1. Introduction

Many ocean structures are supported by large, surface piercing, cylindrical, concrete columns. These columns may be subjected to large and design critical wave slamming loads during their lifetime.

* Corresponding author.
E-mail address: bjornchristian.abrahamsen@sintef.no (B.C. Abrahamsen).

https://doi.org/10.1016/j.jfluidstructs.2022.103804

The industry often carries out scaled wave tank or ocean basin model tests to check both local and global structural integrity. The local shell response, which is the concern of the present paper, is often estimated using finite element analysis (FEA). A relevant way to carry out this type of analysis is to apply wave slamming pressure time series directly onto the finite elements. These pressure time series may come from Froude scaled model tests or class guidelines like (DNV, 2019). It is an open question how this response calculations should be carried out and uncertainties concern; (1) accuracy of the slamming force measurements, (2) scaling of pressures from the model to the full-scale structure, (3) statistical variation of measured wave slamming forces and (4) hydroelastic response. The latter uncertainty being the main subject covered by this paper.

The uncertainties of the slamming force measurement (1) and scaling of slamming loads (2) are both connected to the complexity of the hydrodynamic flow of wave slamming. The measured pressures during slamming may be very local in time and space, which complicates measurements, and the flow can be complicated and involve, for instance, air cavities, air bubbles, acoustic water flow, non-viscous flow separation, ventilation, and cavitation which complicates scaling of pressures from the model to the full-scale structure (Faltinsen, 2006; Faltinsen and Timokha, 2009). The uncertainty related to statistical variation (3) of the measured slamming forces means that stochastic analysis is needed in design. Slamming is a strongly nonlinear phenomenon and probability functions of the amplitudes of relevant response variables must be based on fitting data to a proper stochastic distribution obtained from time-domain numerical simulations or from model tests involving enough realizations of relevant sea states (Næss and Moan, 2012). The uncertainty related to hydroelasticity (4), concerns to what extent the response of the concrete shell affects the hydrodynamic loads, or to what degree the concrete shell responds dynamically. Concerning previous research on marine steel and aluminium structures show that slamming load and response must be analysed as a combination of hydrodynamics and structural mechanics in many cases. In this case the analysis of the hydrodynamic flow and structural reaction, in terms of deflections and stresses, cannot be separated. Hence, there is a mutual interaction between the fluid and the structure where the structural vibrations cause hydrodynamic loads and vice-versa (Faltinsen and Timokha, 2009). Faltinsen and Timokha (2009) shows that the hydrodynamic analysis may be considerably simplified when considering structural responses instead of local hydrodynamic pressures. However, concrete columns are very different than marine steel and aluminium structures and it is an open research question to what extent concrete columns exposed to wave slamming requires thorough hydroelastic analysis.

Knowledge of the local structural response of concrete shells during wave slamming or more idealized slamming events, such as the impact on calm water, is scarce. The present work investigates the local structural response of concrete shells, when dropped from a height and impacting on an undisturbed free surface. This is referred to as a *drop test* in the following text. In this way the fundamental response of concrete shells due to slamming impact is studied under nearly repeatable conditions. The understanding of the fundamentals of the hydroelastic response during drop tests can then be used to motivate simplified and effective analysis procedures for hydroelastic analysis of wave impacts.

A drop test experiment is carried out on a geometrically scaled model, constructed as close as possible to a specific offshore structure, according to Froude scaling laws. This enables the study of how large concrete shells responds to slamming at a practical scale. Furthermore, since Froude scaling laws are applied in the design of the model shells, the same shells can be installed in an ocean basin to study their response due to wave slamming. This latter topic of concrete shell response due to wave slamming is the subject of a follow-up paper.

The hydrodynamic toolbox for slamming contains potential-flow methods, experiments and CFD (Computational Fluid Dynamics) solvers. All these methods can be used in combination with analytical or finite element structural models to analyze the hydroelastic response of concrete shells during calm water impact. In the present work, a simplified method based on a potential flow strip theory and a modal method for the structure is applied to obtain a formulation which is simple and accurate and shows the most important hydrodynamic interaction terms.

The numerical method is inspired by the work by Ionina and Korobkin (1999) who published a 2D mathematical model of a cylinder impacting calm water. The cylinder was modelled using analytical shell theory, and the deflection of the shell was expressed as a sum of dry eigen modes. The hydrodynamics was solved analytically assuming; (1) incompressible, potential flow theory, (2) slamming free surface condition accounting for water uprise, and (3) body boundary conditions enforced at the mean free surface. This means that the flat plate approximation was applied. The validity of this approximations depends on the penetration depth of the cylinder at the time of maximum structural response (strains). The wetted length of the cylinder was solved as part of the coupled mathematical problem. Ionina and Korobkin compared their results to the experimental works of Shibue et al. (1994) and Arai and Miyauchi (1998). These experimental studies were carried out with cylinders with different wet natural periods, meaning that the penetration depth at the time of maximum response was larger in Arai and Miyauchi (1998) than in Shibue et al. (1994) for the same impact velocity. Ionina and Korobkin (1999) shows good agreement between their mathematical method and the stiff cylinder in Shibue et al. (1994) and less accurate agreement with the softer cylinder in Arai and Miyauchi (1998). This is consistent with the fact that the flat plate approximation is expected to be less accurate for larger penetration depths. Sun and Faltinsen (2006) solved the cylinder impact problem using a theory similar to Ionina and Korobkin (1999), and also with a more accurate hydrodynamic model maintaining nonlinear boundary conditions and was not able to explain the difference between Ionina and Korobkin's (1999) method and the experiments in the case of the soft cylinder (Arai and Miyauchi, 1998) by the simplifications introduced in the hydrodynamical model. The works in Ionina and Korobkin (1999) and Sun and Faltinsen (2006) suggest that the hydrodynamic problem can be significantly simplified and may still provide accurate results.

Other research on steel and aluminium structures provides important hypotheses for the present work. Faltinsen (1999) studied theoretically the hydroelastic problem of a wedge consisting of a stiffened plate. Orthotropic plate theory was used for the stiffened plates and strip theory based on Wagner's theory (Wagner, 1932) was used to model the flow of water. The hydro-elastic effect was defined as the ratio between the magnitude of strain when hydroelasticity was accounted for, divided by the magnitude of strain when the structure was loaded statically. This fraction is often referred to as the dynamic amplification factor, DAF. The resulting plot, (see (Faltinsen, 1999) Fig. 17) shows similarities with that of dynamic amplification of a single degree of freedom system exposed to transient loads (See e.g. Clough and Penzien, 1975 p 94). The structural response (strain maxima) is governed by the load duration compared to the wet natural period. When the duration of the load is short compared to the natural period (impulse response) the strain maxima are proportional to the impact velocity. In the limit as the load duration goes to zero, the analysis in Faltinsen (1999) is equivalent to the response of a horizontal beam undergoing free vibrations, at the wet natural frequency. In this case, Faltinsen (1997) showed that the proper initial condition for the beam was that the spatially averaged initial beam deflection velocity was equal to the impact velocity. Only one structural mode was considered, and the maximum strain occurred at one quarter of the wet natural structural period. The theoretical results by Faltinsen (1997) were experimentally validated.

The overall objective of this work is to improve the understanding of the local response of large concrete columns when exposed to both wave and drop test impacts. To study these problems experimentally in full-scale is both expensive and impractical. To enable both model tests in ocean basins, and drop tests at a practical scale, we study slamming of concrete shells at a scale of 1:55 assuming Froude scaling.

Hence, there is a need to create an approximate Froude scaled model shell, which allows for measuring the structural response directly under Froude scaled conditions. To do so, the fundamental Froude scaling principles of thin elastic shells needs to be established. Furthermore, a proper Froude scaled elastic shell needs to be constructed out of available materials and drop tested before tested in waves. Furthermore, there is a need to understand the role of hydroelasticity of concrete shells in terms of dynamic amplification factors in a similar fashion as presented in Faltinsen (1999) for steel and aluminium structures. For engineers who estimates the structural response based on slamming force measurements, which are most often measured on nearly rigid surfaces, it is particularly relevant to understand how the hydrodynamic loads are modified by the structural response. These load modifications, if important, needs to be accounted for in FEA response calculations.

The following sections address the research tasks listed above. In Section 2, the fundamental Froude scaling principles of thin elastic shells are elaborated, and simplifications of these principles are introduced to allow for construction of approximate Froude scaled elastic shells from available materials. These Froude scaled elastic sections representing concrete are, to the authors knowledge, the first of its kind and enable the study of the fundamental concrete shell response due to both calm water and wave impacts. The latter being the topic of a future paper.

The drop test experiment is described in Section 3. The numerical method is presented in Section 4 and compared with the experimental measurements in Sections 5 and 6. The numerical method is applied to both the model shells at a geometric scale of 1:55 and to the large concrete shells at prototype scale (1:1) in order to quantify how accurately the response of the approximate Froude scaled model shells represents the response of full-scale concrete shells (See Sections 5–7). The effect of hydroelasticity is studied through dynamic amplification factors in Section 8. Finally, the hydrodynamic load modifications due to structural response for concrete shells are presented in Section 9. Results presented in this paper are relevant for full-scale concrete shells, and hence the data are presented in full-scale values. In the parts of the paper where model scale data are relevant this is explicitly stated.

This research shows how realistic Froude scaled elastic shells representing concrete shells can be designed. Furthermore, the results show that even large, thick and heavy concrete shells experience significant hydroelastic effects during slamming. Hence, the structural responses are seen to significantly modify the hydrodynamic loads during impact. These load modifications should be properly accounted for when designing concrete shells exposed to slamming.

2. Scaling strategy of concrete shells exposed to wave impact

Fig. 1(a) shows a monopile during model tests in an ocean basin at a geometric scale of 1:55 exposed to a steep and high wave. The full-scale monopile has a diameter of 31 m. The model test is carried out to study the local structural shell response due to wave impact. Only a part of the cylinder which is facing the wave is considered elastic while the rest of the cylinder is assumed rigid. The elastic section indicated in Fig. 1 is 24.6 m tall, with the lower edge at the mean free surface. The concrete section spans a sector of 77.3 degrees of the cylinder.

The full-scale shell was constructed in reinforced and prestressed lightweight concrete. Fig. 2 shows the generalized design. The concrete wall was reinforced with an inner and outer reinforcement layer (dashed lines) consisting of 10 steel bars with diameter of 25 mm per meter in both the hoop direction and vertical direction. The prestressing reinforcement is in the centre of the cross-section (black line), made of steel wires. The concrete wall is prestressed with a membrane force of 4.0 mN/m in both the vertical and the hoop direction.

Concrete shells are often analysed as a homogeneous shell with a linear elastic material model. In the present work an effective Young's modulus of 30 GPa is assumed. Furthermore, the average density and Poisson's ratio of the full-scale concrete is equal 2300 [kg/m^3] and 0.20 [–], respectively.

The modelling of concrete is subject to standards like (NS3473, 2003; FIB, 2010). One uncertainty of the linear elastic material model is that the Young's modulus depends on the rate of strain (FIB, 2010). This effect depends on the type of

Fig. 1. (a) Wave hitting a monopile during a scaled ocean basin model test at 1:55. (b) A local approximate Froude scaled model shell representing concrete covering a section of the column with a local elastic section.

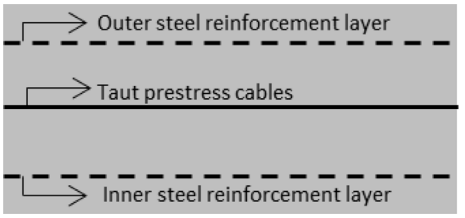

Fig. 2. The cross section of the reinforced and prestressed lightweight concrete shell considered in this work.

concrete considered. For relevant strain rates relevant for wave slamming the effective Young's modulus may be increased by up to 20% (FIB, 2010). For the present calculations, the Young's modulus is increased by 10% to account for the effect of strain rate. As the present work focus on the fluid structure interaction aspects of concrete response, a linear elastic material model is sufficient.

The following text describes the general scaling principles for thin concrete shells when exposed to wave slamming loads. To arrive at the elastic scaling principles for thin elastic shells, it is reasonable to consider an idealized impact governed by hydrodynamic flow conditions which follow Froude scaling. Hence, the water is assumed incompressible, inviscid and the flow is irrotational. Furthermore, free-surface tension is neglected. This means that potential flow theory is valid. The scaling problem of the elastic shell is studied through nondimensionalization of a relevant set of equations describing the physics of the problem, which in turn leads to identification of nondimensional numbers. In order for the nondimensional mathematical problem to be equal for two scales it requires that a set of nondimensional numbers are equal at the two scales.

For the problem of the wave impacting the elastic shell section in Fig. 1, the time instant just before the wave touches the elastic section of the cylinder is denoted $t = 0$. Important nondimensional parameters before $t \leq 0$ and during $t > 0$ the impact are elaborated next.

The velocity potential of the water flow can be found through a boundary value problem consisting of the following equations: (1) Laplace's equation for the water domain, (2) Bernoulli's equation for the pressure on the free surface, (3) The kinematic free surface condition and (4) kinematic boundary conditions at the wetted surface of the cylinder. When this boundary value problem is made nondimensional, it allows for identification of important non-dimensional parameters which needs to be equal in model and full-scale for the scaling to be valid. Only Bernoulli's equation provides a nondimensional number, which is the Froude number. This implies that the characteristic wave impact velocity U follows Froude scaling. In addition, the model and full-scale cylinder needs to be geometrically scaled, meaning that all external dimensions of the structure, like height and radius, needs to be a factor $1/\lambda$ smaller in model scale. Here, λ is the geometrical scaling factor, which in this work is 55.

When the wave touches the elastic shell ($t > 0$), the water and the structure start to interact. The hydrodynamic pressure relates to the dynamic equilibrium equation of the elastic shell at its surface. Thin shell theory can be used to describe the deformations of the full-scale concrete shell. Leissa (1973) presents the dynamic equilibrium equations for a thin circular cylindrical shell. The equation of motion for the normal displacement of the shell is according to (Leissa, 1973 Eqs. (2)–(7)):

$$\rho_c h \frac{\partial^2 w}{\partial t^2} + D\frac{\partial^4 w}{\partial x^4} + \frac{2D}{R^2}\frac{\partial^4 w}{\partial \theta^2 \partial x^2} + \frac{D}{R^4}\frac{\partial^4 w}{\partial \theta^4} + \frac{K}{R^2}w + \frac{\nu K}{R}\frac{\partial u}{\partial x} + \frac{K}{R^2}\frac{\partial \mathrm{v}}{\partial \theta} = -p. \tag{1}$$

Here, u, v and w are the displacements of a point on the shell in the axial (x-direction), circumferential (θ-direction) and radial direction, respectively. The cylindrical coordinate system is indicated in Fig. 1(b). Furthermore, h is the shell thickness, R is the shell radius, $K = Eh/\left(1-\nu^2\right)$ and $D = Eh^3/[12\left(1-\nu^2\right)]$. Here E is Young's modulus and ν is Poisson's ratio. p is the hydrodynamic pressure on the cylinder surface and ρ_c is the density of the concrete shell. This equation is made nondimensional using the impact velocity U and the radius of the column R in order to identify relevant nondimensional parameters. The equation is divided by ρU^2 where ρ is the water density. Furthermore, u, v, w are made nondimensional with respect to R. Time, t, is made non-dimensional with the factor R/U. Then the following nondimensional parameters are identified,

$$I_1 = \frac{\rho_c h}{\rho R}, \quad I_2 = D/(\rho U^2 R^3), \quad I_3 = \frac{K}{\rho U^2 R} \quad and \quad I_4 = \nu. \tag{2}$$

Nondimensionalising the two other shell equilibrium equations for circumferencial (hoop) and axial displacements (Leissa, 1973 Eqs. (2)–(7)) does not provide additional nondimensional numbers. The solution of the nondimensional mathematical problem is equal when the nondimensional numbers 1–4 are equal for the model and the full-scale problem. This can be achieved if; $R = \lambda\overline{R}$, $E = \check{r}\lambda\overline{E}$, $h = \lambda\overline{h}$, $\rho_c h = \check{r}\lambda\overline{\rho}_c\overline{h}$, $\nu = \overline{\nu}$, $\rho = \check{r}\overline{\rho}$. Here, $\check{r}$ is the salt-water to fresh-water density ratio, $\check{r} = \rho/\overline{\rho}$, and variables with a bar indicates model scale parameters.

Manufacturing a scaled model shell which satisfies these conditions depend on (1) what materials and manufacturing techniques which are available, (2) the required geometrical scale factor λ, and (3) the dimensions and material properties of the full-scale concrete shell. For a scaling factor of 1:55 the ideal material would have a correct scaled modulus of elasticity equal to 30 GPa/55/1.024 = 0.53 GPa. A reliable material could not be identified with this low Young's modulus. Hence, it was impossible to obtain equal nondimensional numbers I_1, I_2, I_3 and I_4. To simplify the modelling, the importance of the different non-dimensional numbers in Eq. (2) were studied to identify their relative importance. For the impact on calm water the slamming load is largest initially and decays with time. This means that the slamming load acts in a relatively small area along the vertical centreline of the shell facing the wave. For this type of load, it is relevant to study the analytical solution of a shell with a static point load presented by Timoshenko and Woinowsky-Krieger (1959) p 501 (originally proposed by Lord Rayleigh). For this theory to be valid, the boundaries of the circular cylinder are free at both ends. The analytical solution depends on the plate bending stiffness D, and the Poisson ratio ν. Based on this analytical solution, D (bending stiffness) is considered more important than K (membrane stiffness) and ν. Furthermore, since concrete shells are relatively heavy—with a structural mass comparable to the local added mass effect experienced during slamming, it was found important to maintain the correct mass per area of the shell. This assumption was confirmed when studying the modal mass force and added mass force for three impact velocities V=10, 16 and 24 m/s for the dominant mode of vibration. These modal forces are plotted in Fig. 26 and show that structural modal mass force is roughly 50% of the added mass force for $t > 0.6T_d$, where T_d is the dominant dry natural period of the shell. This means that the structural mass is significant and must be modelled accurately. Based on these arguments the nondimensional parameters I_1 and I_2, were found more important than I_3 and I_4 in Eq. (2). This assumption is studied in detail later through comparisons of numerical simulations of the model shells and the full-scale shells in Sections 5–8.

To further minimize shell scaling errors, a material was selected with as low Young's modulus as possible (but not smaller than 0.53 GPa). This material was polycarbonate (PC) which has a typical Youngs modulus ranging from 2.0 to 2.5 GPa. The mechanical properties of polycarbonate are not sensitive to small temperature variations, see Cao et al. (2014). It is also easy to form, and it can sustain large deformations without permanent deformations. In the present experiment polycarbonate plates with thicknesses of 6 mm and 9.5 mm were used. The corresponding full-scale concrete thicknesses were found through the equation:

$$\frac{D}{\overline{D}} = \check{r}\lambda^4. \tag{3}$$

The corresponding full-scale thickness following the scaling of the bending stiffness were 584 mm and 872 mm. Dedicated tensile tests were carried out according to ISO 527-1 (ISO, 2019) to properly document the material properties of polycarbonate. Dog bone test specimen were cut from the same flat plate as used for the model test in both the axial and the circumferential direction. Six tensile tests were carried out for each of the two plate thicknesses and directions to measure the Young's modulus. The tensile tests showed small directional dependency (anisotropy) on the Young's modulus in the range of strains measured during the drop tests, which was up to 0.2%.

Fig. 3 shows the stress strain curves for both the 9.5 mm and the 6 mm polycarbonate. The average Young's modulus was estimated at 0.25% strain: 2.1 GPa for the thick polycarbonate and 2.5 GPa for the thin polycarbonate. The 12 measured stress strain curves are plotted and shows that the test-to-test variability is larger for the thin 6 mm plate than for the 9.5 mm plate. Four separate tensile tests using digital image correlation (DIC) was used to derive the Poisson's ratio of the material. The contactless DIC technique were preferred over traditional transverse clip-on extensometers since the latter tend to cause significant bending of soft polymer tensile samples. The Poisson's ratio was estimated to be 0.43 for the polycarbonate. The strain rate of the plate reached a maximum of about 3 [1/s] in the drop test experiments. The effect of strain rate for polycarbonate was studied by Cao et al. (2012), who tested experimentally the strain rate effect for a large range of strain rates. The results show that the effect of strain rate is not significant for the present work.

To shape the test specimen, the plates were dried, and shaped through drape-forming in an oven at approximately 160 degrees Celsius. Fig. 4(a) shows the measured difference between the actual radius r of the thin shell and the targeted

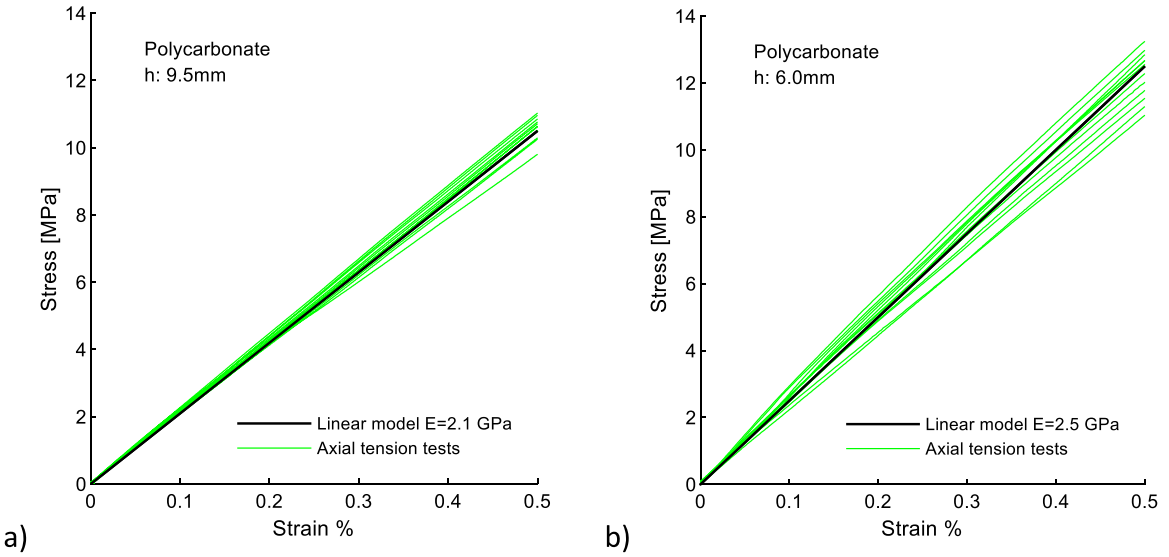

Fig. 3. Nominal stress–strain curves from uniaxial tensile tests for the (a) 9.5 mm and the 6.0 mm polycarbonate plates used for the Froude scaled elastic model shells.

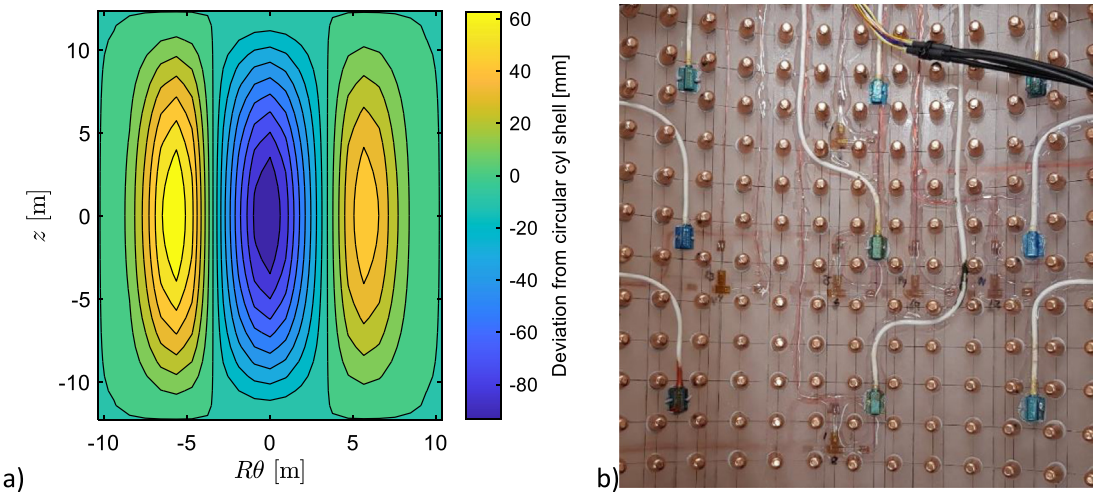

Fig. 4. Plot (a) shows the measured radial shape of the thin polycarbonate shell, $\boldsymbol{r} - \boldsymbol{R}$, when scaled to full-scale dimensions. The maximum radial imperfection is 90 mm/31 000 mm=2.9‰. Photograph (b) shows the inside of the polycarbonate shell with revolver bullets used to ballast the shell to the correct scaled mass. The accelerometers are blue and placed in a 3 x 3 matrix. The strain gauges measure the strain in the hoop and longitudinal directions in six different points on the plate. (For interpretation of the references to colour in this figure legend, the reader is referred to the web version of this article.)

radius R (full-scale value). The production error shows a trough with a maximum depth of 90 mm (full-scale value) in the middle of the shell while the plate is distorted outwards on both the left and right side. The effect of the imperfection on the calculated results are quantified later in this paper through hydroelastic calculations.

The polycarbonate shells needed to be ballasted to obtain the correct mass per square meter of the shell $\overline{m}$ according to the following scaling law:

$$\frac{m}{\overline{m}} = \check{r}\lambda \tag{4}$$

For this purpose, revolver bullets were glued to the inside of the plate. 8.1-g bullets with a diameter of 9.09 mm was mounted on the inside of the thin 6 mm shell while 12.95-g bullets with diameter of 10.9 mm were glued on the inside of the thick 9.5 mm plate. The distance between the bullets were 22.5 mm for both shells. Fig. 4(b) shows the configuration of the bullets mounted on the inside of the shell. The equivalent material properties of the scaled elastic model shells are compared to the material properties of the full-scale concrete shells in Table 1.

Table 1
The material properties of reinforced lightweight concrete and the model scale ballasted polycarbonate shells. The full-scale thicknesses are calculated based on Froude scaling the bending stiffness of the shell.

Scale:	Units	Thick shell			Thin shell		
55		Full-scale specification	Full-scale as modelled	Model scale as modelled	Full-scale specification	Full-scale as modelled	Model scale as modelled
Young's mod.	GPa	30		2.1	30		2.5
Poisson's ratio	[–]	0.20	0.43	0.43	0.20	0.43	0.43
Density	kg/m^3	2300	2391	1200	2300	2241	1200
Thickness	mm	872	872	6.0	584	584	9.5
Mass per area	kg/m^2	2006	2085	36.98	1342	1308	23.2

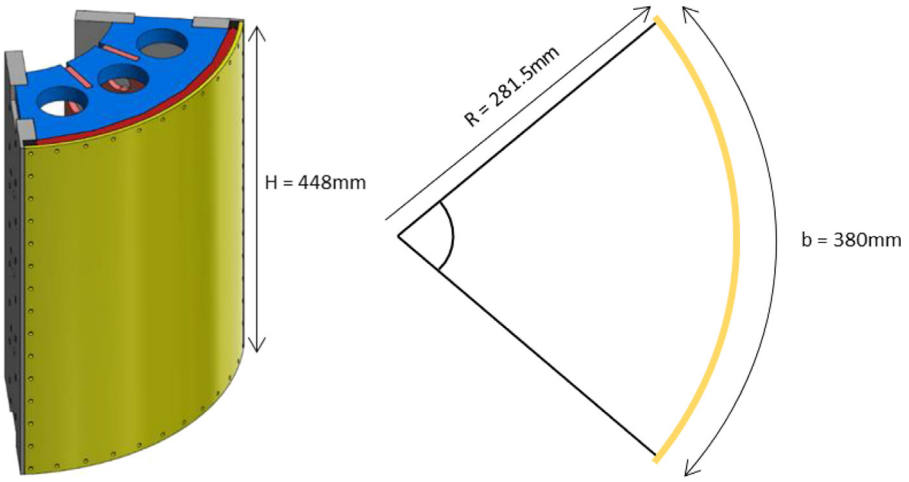

Fig. 5. The Froude scaled elastic concrete section (yellow) bolted onto a stiff aluminium frame. *H* and *b* are measured from centre to centre of the corner bolts of the shell. Model scale dimensions. (For interpretation of the references to colour in this figure legend, the reader is referred to the web version of this article.)

The Froude scaled elastic concrete shells were mounted onto the stiff aluminium frame shown in Fig. 5. The elastic shell was bolted to the frame using 12 bolts along each of the curved edges and 15 bolts along each of the straight edges. The outer surface of the shell was part of a circular cylindrical surface with radius of 281.5 mm (model scale value). The elastic shell was 380 mm wide and 448 mm tall measured from centre to centre of the corner bolts attaching the shell to the frame (model scale values).

HBM Type 3/350 LY18 strain gauges with a measurement area of 3×1.6 mm^2 were mounted on the elastic sections. The strain gauges were mounted in pairs on the inside and outside surfaces, in the hoop and vertical direction of the shell to document the bending moment and membrane force at six different measurement points. The locations of these measurement points were selected based on experience from Wåsjøet al. (2017) which showed that; (1) the dominant deflection shape have several half waves in the circumferential direction while only one half wave in the axial direction of the shell, (2) the magnitude of bending moments and axial forces are expected to be larger in the circumferential direction than in the axial direction and (3) the largest bending moments are located in the centre of the shell. From this perspective, four measurement points were instrumented in the middle of the shell along the circumferential direction and three points along the front of the shell in the vertical direction.

Fig. 6(a) shows the numbering system (1–6) and plot (b) shows the location of these measurement points as red squares in mm (model scale values). Nine Meggitt 7264B-2000 accelerometers were also attached to the inside of the plate, the numbering system and coordinates of these points are shown as blue squares in Fig. 6. These accelerometers were designed for crash testing and has a resonance frequency of 28 kHz and a range of 2000 g. The mass of one accelerometer was measured to 0.8 g, and the mass of the accelerometer cable between two ballast bullets (22 mm) was measured to 0.25 g. The mass of the accelerometers introduced a local mass error on the nine 22×22 mm^2 areas on which they were mounted. The mass of the polycarbonate plate and ballast bullets can be found in Table 1. Based on these data the mass error on the nine 22×22 mm^2 areas were estimated to 9.4% for the thin shell and 5.9% for the thick shell. This extra mass was considered small and was neglected in all numerical calculations in this paper. The strain gauge and accelerometer measurements were both sampled at a frequency of 19.2 kHz (model scale value). In addition, the signals were filtered at a frequency of 2 kHz (model scale value).

The membrane forces and bending moments were derived from the strain measurements assuming thin shell theory (Timoshenko and Woinowsky-Krieger, 1959). The moments and membrane forces are shown in full-scale values in this

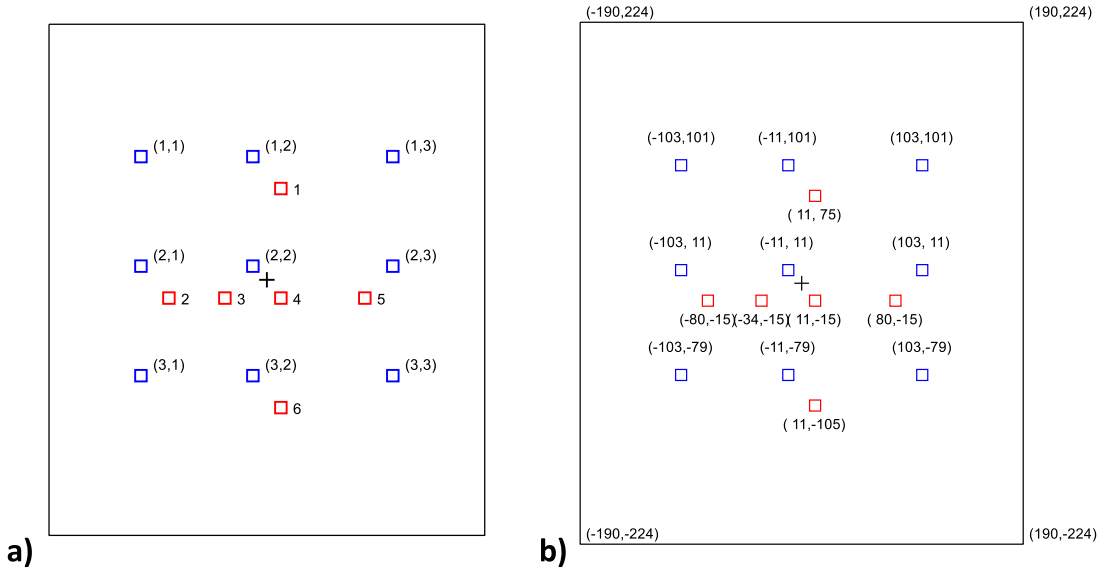

Fig. 6. Location of accelerometers (blue) and strain measurement points (red). (a) numbering. (b) location of measurement points in (s,z) coordinates where the centre of the coordinate system is in the middle of the section $(+)$ and s follows the surface of the shell in the horizontal direction. The shell is seen from the outside (wet side). (For interpretation of the references to colour in this figure legend, the reader is referred to the web version of this article.)

report since the results are most relevant for full-scale concrete shells. The full-scale hoop bending moment per unit width is:

$$M_\theta = \left[\varepsilon_\theta^{in} - \varepsilon_\theta^{out} + \nu\left(\varepsilon_z^{in} - \varepsilon_z^{out}\right)\right] \frac{Eh^2}{12\left(1-\nu^2\right)} \frac{\check{r}\lambda^3}{10^9}. \tag{5}$$

The hoop bending moment is positive when there is a positive strain (tension) inside the shell and a negative strain (compression) on the outside of the shell. The bending moment per meter is in full-scale units; [kNm/m]. The membrane force per meter in the hoop direction is:

$$N_\theta = N_{pt} + \left[\varepsilon_\theta^{in} + \varepsilon_\theta^{out} + \nu\left(\varepsilon_z^{in} + \varepsilon_z^{out}\right)\right] \frac{Eh}{2\left(1-\nu^2\right)} \frac{\check{r}\lambda^2}{10^{12}}. \tag{6}$$

The membrane force is positive when the plate is in tension, and negative when compressed. The membrane forces are in full-scale units; [mN/m]. Both the bending moments and the membrane forces are calculated based on the measured strains. Furthermore, the pretension $N_{pt} = -4.0$ mN/m is added to the membrane force to account for pretension caused by the taut cables in the shell (See Fig. 2). The corresponding formulas for the bending moments and membrane forces in the z-direction is found by substituting z for θ in the above equations.

3. Set up of water impact experiment

Fig. 7(a) shows the set-up of the drop tests. A rotating arm was mounted on hinges on the left side. The arm was rotated upwards and released to rotate freely until the elastic section hit the calm water surface. The set up with the rotating arm was identical to the set-up of the tests by Abrahamsen et al. (2020). The impact velocity was defined as the vertical component of the velocity at the front of the shell (point A) at the time of impact. The impact velocity was derived from both energy conservation and by integration of accelerometers mounted on the frame, as explained by Abrahamsen et al. (2020). Fig. 7(b) shows the impact velocity in full-scale as a function of drop height in model scale. The blue curve shows the theoretical impact velocity derived from energy conservation. The red dots show the measured impact velocity derived from accelerometers as a function of the measured drop height for the tests with the thick elastic shell. Table 2 lists the drop tests for the thin and the thick elastic shells.

Fig. 8(a) and (b) shows the measured hoop directional bending moment and hoop membrane force near the centre of the shell at pt. 4. These drop tests were carried out with impact velocity of 12.2 m/s with the thick elastic model shell. The plot shows that the elastic shell vibrates with a governing frequency of about 23 Hz. More of the physical aspects of the impact are discussed together with numerical simulations in Section 5. The plots in Fig. 8 shows the test used for comparison with the numerical method, test 9, together with three repetition tests 10, 11 and 12. To give an overview of the repeatability for all 6 measurement points the extreme hoop bending moment max|M| and extreme hoop membrane

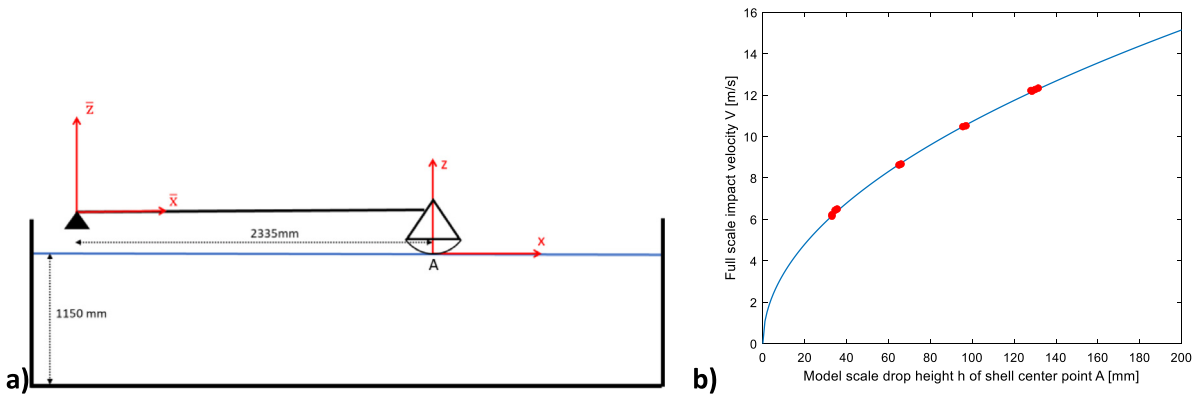

Fig. 7. (a) The drop test set up showing the hinged arm and the frame holding the elastic model shells. (b) Estimated Impact velocities based on; theoretical energy conservation (blue curve) and integration of accelerometer mounted on the drop rig (red dots). Drop heights are in model scale, while impact velocities are given in full-scale. (For interpretation of the references to colour in this figure legend, the reader is referred to the web version of this article.)

Table 2
Test programme for the thick and thin Froude scaled elastic concrete shells. The impact velocity was estimated from integration of acceleration measurements.

Test no:	V (m/s)	Shell	Test no:	V (m/s)	Shell
1	6.23	Thick	25	5.90	Thin
2	6.44	Thick	26	5.92	Thin
3	6.50	Thick	27	5.98	Thin
4	6.15	Thick	28	8.68	Thin
5	8.63	Thick	29	8.97	Thin
6	8.67	Thick	30	8.71	Thin
7	10.52	Thick	31	10.70	Thin
8	10.48	Thick	32	10.64	Thin
9	12.19	Thick	33	10.67	Thin
10	12.34	Thick	34	12.14	Thin
11	12.27	Thick	35	12.12	Thin
12	12.22	Thick	36	8.57	Thin
21	11.76	Thin	37	8.34	Thin
22	12.21	Thin	38	6.02	Thin
23	8.65	Thin	39	6.12	Thin
24	8.73	Thin			

force max|N| were calculated for the same four repetitions tests. These extremes are plotted as bars in Fig. 8(c) and (d). The repetition error was estimated as the coefficient of variation COV defined as the standard deviation of the extremes to the mean of the extremes. The COV was all less than 2.7% for the extreme hoop bending moments and 2.8% for the extreme hoop membrane force for all six measurement points. These estimates of repeatability (COV) are uncertain due to limited number of repetitions. However, the low COVs indicate that repeatability is not an important concern when comparing results with numerical calculations.

The measurement errors of strain gauges originate from different sources like the strain gauge itself, amplifier and acquisition set up and that the strain of the material is not fully transmitted to the strain gauge. From previous experience error from strain gauges are in the order of 1 to 2%. Before the drop tests the straight edge of the test sections were clamped to the edge of a table and loaded with a mass hanging from the other straight edge of the elastic section. From these tests the largest strain errors were between 5%–10% compared to FEA. However, this test contained uncertainties beyond that of the strain gauge itself, like for instance the level of clamping of the edge and uncertainty related to the Young's modulus of the polycarbonate entering the FEA. Furthermore, the calculated shell bending moments and membrane forces, which were derived from the measured strains are proportional to the Young's modulus of the polycarbonate. The material tests reported in Fig. 3 shows that the uncertainty of the Young's modulus is in the order of ±5%. This material uncertainty is larger for polycarbonate than for construction steel and aluminum. These measurement and material errors should be considered when comparing the experimental measurements and numerical calculations.

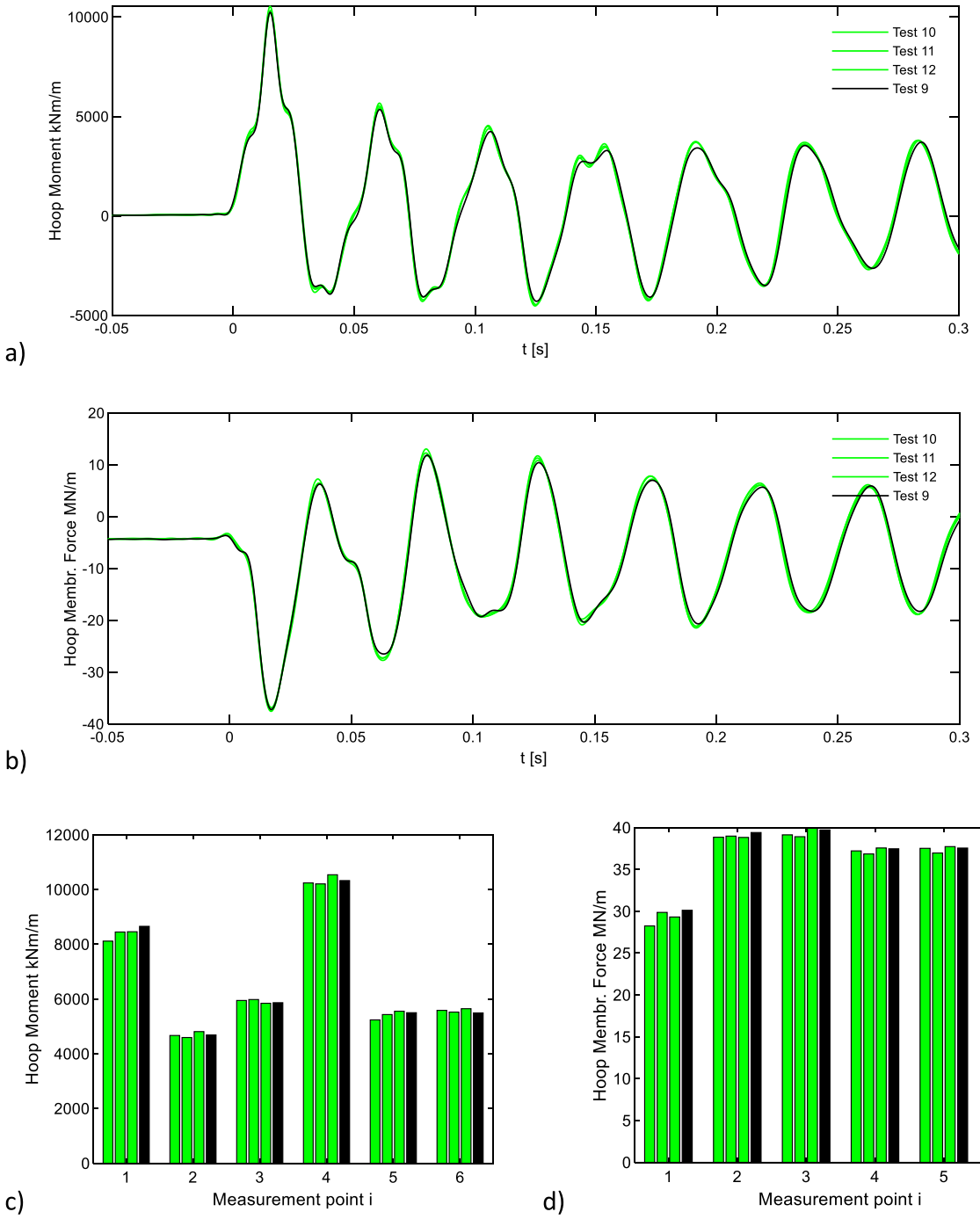

Fig. 8. Plot (a) and (b) shows the measured hoop bending moment and hoop membrane force at the centre of the shell (pt. 4) in the thick elastic model shell. The four different drop tests, 9, 10, 11, 12 were carried out with an impact velocity of 12.2 m/s to document the repeatability of the drop test measurements. Plot (c) and (d) shows the measured extreme bending moments and membrane forces, max|M| and max|N| for all 6 measurement points for the same tests.

4. Hydroelastic theory for concrete shells

Fig. 9 shows a curved shell impacting a calm free surface during a drop test. The shell is fixed along all boundaries and the panel is curved with a radius of curvature equal to R before impact. The shell is discretized into finite elements.

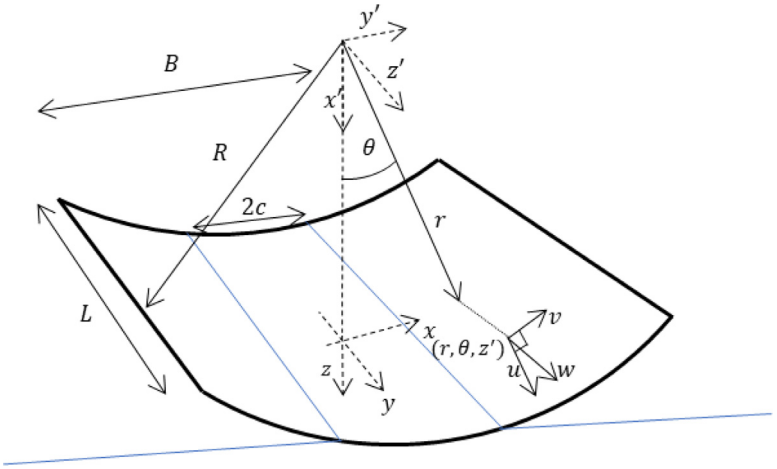

Fig. 9. Coordinate system of the shell $(\boldsymbol{r}, \boldsymbol{\theta}, \boldsymbol{z}')$ and coordinate system for the hydrodynamic load $(\boldsymbol{x}, \boldsymbol{y}, \boldsymbol{z})$.

The element nodes are defined in a cylindrical coordinate system (r, θ, z') which is defined relative to the coordinate system (x', y', z'), with the x' axis pointing downwards. The displacement of the nodes (u, v, w) is the displacement in the radial (r), hoop (θ) and longitudinal (z') direction of the shell. The three corresponding rotations of each node of the mesh are defined according to the right-hand rule. The displacement and rotations of each node is collected in the nodal displacement column vector $\{D\}$. The equation of motion is written as:

$$\left[\overline{M}\right]\left\{\ddot{D}\right\} + \left[\overline{K}\right]\{D\} = \left\{R^{ext}\right\}. \tag{7}$$

Here, $\left[\overline{M}\right]$ is the mass matrix, $\left[\overline{K}\right]$ is the stiffness matrix and $\left\{R^{ext}\right\}$ is the load vector and dot mean time derivative. The equation system is the reduced system after boundary conditions are accounted for. The dry eigenvalue problem is solved using the finite element (FE) software (Nastran, 2019). The shell is discretized into rectangular four noded shell elements (Nastran element formulation: quad4). The response is then expressed in terms of several dry natural modes $\overline{D}_i$, which are collected in a matrix:

$$[\Psi] = \left[\overline{D}_1 \overline{D}_2 \ldots \overline{D}_n\right]. \tag{8}$$

The nodal displacement column vector $\{D\}$ is expressed in terms of these modes, with modal amplitudes stored in the column vector $\{Z\}$ in the following way,

$$\{D\} = [\Psi]\{Z\}. \tag{9}$$

The modal equations follow:

$$[M]\left\{\ddot{Z}\right\} + [K]\{Z\} = \{R\}. \tag{10}$$

Here, $\{R\} = [\Psi]^T \left\{R^{ext}\right\}$ and $[M] = [\Psi]^T [\overline{M}][\Psi]$ and $[K] = [\Psi]^T [\overline{K}][\Psi]$ are diagonal mass and stiffness matrixes. The nodes along the boundary of the shell, coincides with the location of the bolts for the reference FE mesh. By dividing the sides of the elements by a mesh refinement factor (*mrf*) equal to 2, 4 and 8, refined meshes are obtained. At the FE nodes corresponding to the location of the bolts, the nodes are fixed in all rotations and displacements. The nodes on the boundary of the shell located between the bolts were fixed in the following way along the vertical straight edges: translations (r, θ,z): fixed, free, free and rotations (r, θ,z): free, fixed, free; and for the curved edges: translations (r, θ,z): fixed, free, free and rotations (r, θ,z): free, free, fixed.

The hydrodynamic problem is solved assuming incompressible potential flow theory. The velocity potential is expressed in the following way:

$$\phi = \varphi_0(x, y, z; t)\dot{Z}_0(t) + \sum_{j=1}^{N_m} \varphi_j(x, y, z; t)\dot{Z}_j(t). \tag{11}$$

Here, $\dot{Z}_0(t) = V_0$ and $\dot{Z}_j(t)$ are the unknown modal amplitude velocity of mode j and $\dot{Z}_0(t)$ is the rigid body velocity during the impact which was measured during the experiments.

The measured rigid body velocity of the frame during impact is shown in Fig. 10. The blue curves show the nondimensional rigid body impact velocity, and the red curves show the nondimensional deflection velocity as a function of time for the thick elastic shell for the impact velocity of ∼12.2 m/s. The rigid body velocity shows less than 3% reduction

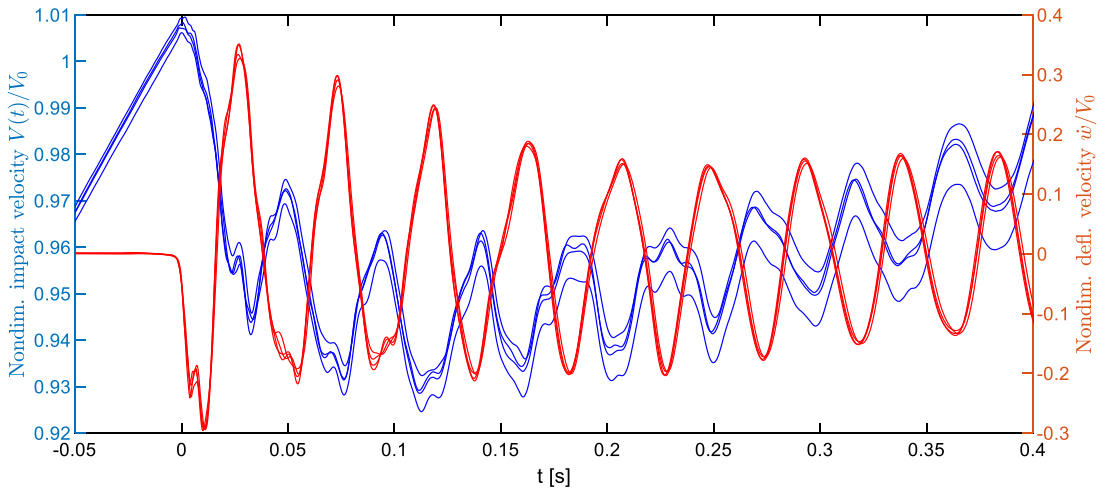

Fig. 10. Experimental nondimensional rigid body velocity (blue) and nondimensional deflection velocity near the centre of the shell at pt. 2–2 (red) as a function of time. The plot shows the measurements of four different repetitions of the impact. (For interpretation of the references to colour in this figure legend, the reader is referred to the web version of this article.)

at the time of maximum deflection, which corresponds to the first zero up-crossing of the red curve. Based on this argument the rigid body velocity is assumed constant during the impact, meaning that $\dot{Z}_0(t) = V$ for the calculations.

The coordinate system is fixed at the mean free surface, with z pointing downwards (see Fig. 9). The kinematic body boundary conditions are, $\nabla\phi_0 \cdot \boldsymbol{n} = n_3$ and $\nabla\phi_j \cdot \boldsymbol{n} = \Psi_j^{(n)}$ for $j = 1, 2, \ldots, N_m$, which should be imposed on the exact wetted surface of the cylinder. Here $\boldsymbol{n}$ is the unit normal vector of the shell surface pointing into the water domain and $\Psi_j^{(n)}$ denotes the normal component of the deformation of mode j at the wetted surface of the cylinder. However, in this work the body boundary conditions are imposed according to the flat plate approximation. This means that the body boundary condition is written as $\varphi_{0z} = 1$ and $\varphi_{jz} = \Psi_j^{(n)}$ for $j = 1, 2, \ldots, N_m$ and is imposed on $z = 0$. The pressure was found through the linearized Bernoulli's equation, $p = -\rho\phi_t$. The modal load was then:

$$R_i = -\iint_S p\Psi_i^{(n)} dS. \tag{12}$$

Here S means the wetted surface of the elastic shell. Since the velocity potential is zero on the mean free surface, we can interchange the time derivative in the integrand with the time derivative of the integral. That means R_i is,

$$R_i = \rho\frac{\partial}{\partial t}\iint_S \left(\varphi_0(x,y,z;t)\dot{Z}_0(t) + \sum_{j=1}^{N_m}\varphi_j(x,y,z;t)\dot{Z}_j(t)\right)\Psi_i^{(n)}\, dS \quad for \quad i = 1, \ldots, N_m. \tag{13}$$

The added mass coefficients are identified as,

$$A_{i0} = -\rho\iint_S \varphi_0(x,y,z;t)\,\Psi_i^{(n)}\, dS, \quad for \quad i = 1, \ldots, N_m, \tag{14}$$

and

$$A_{ij} = -\rho\iint_S \varphi_j(x,y,z;t)\,\Psi_i^{(n)}\, dS, \quad for \quad i = 1, \ldots, N_m,\ j = 1, \ldots, N_m. \tag{15}$$

The hydrodynamic modal force is then written as,

$$R_i = -\frac{\partial}{\partial t}\left(A_{i0}\dot{Z}_0(t)\right) - \sum_{j=1}^{N_m}\frac{\partial}{\partial t}\left(A_{ij}\dot{Z}_j(t)\right). \tag{16}$$

The modal force is then,

$$\{R\} = -\left\{\dot{A}_0\right\}V - \left[\dot{A}\right]\left\{\dot{Z}\right\} - [A]\left\{\ddot{Z}\right\}. \tag{17}$$

The first term is the modal slamming force for a rigid plate. The second term is proportional to the impact velocity and the modal response velocity and is denoted the slam damping term. The third term is the time dependent added mass term.

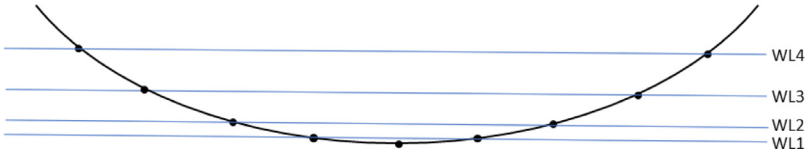

Fig. 11. The hydrodynamic added mass is estimated on a set of water lines intersecting the finite element nodes.

The intersection line between the free surface and the shell during the impact is assumed to be rectangular and independent of the deformation of the shell. The wetted area is defined by the parameter $c(t)$ in Fig. 9. During the wetting of the shell surface the wetted length $c(t)$ is found from Wagner's theory (Wagner, 1932), then when the shell is fully wetted c is assumed constant and equal to half the width of the section B. These conditions are written as:

$$\begin{aligned} &c = 2\sqrt{RVt},\ \dot{c} = V\sqrt{\frac{R}{Vt}} \quad \text{for } c \le B/2 \\ &c = B/2,\ \dot{c} = 0 \qquad\qquad \text{for } c > B/2. \end{aligned} \tag{18}$$

The hydrodynamical boundary value problem is solved for many drafts as shown in Fig. 11. These drafts are chosen such that the water line coincides with the finite element nodes. When the FE mesh is refined by a factor 2 then the number of drafts in the calculation of the added masses increases by the same factor. This means that the load time history is refined when the mesh is refined.

Combining Eqs. (17) and (18) leads to the following coupled hydroelastic modal equation system:

$$([\mathbf{M}] + [\mathbf{A}])\left\{\ddot{\mathbf{Z}}\right\} + ([\mathbf{B}] + \left[\dot{\mathbf{A}}\right])\left\{\dot{\mathbf{Z}}\right\} + [\mathbf{K}]\{\mathbf{Z}\} = -\left\{\dot{\mathbf{A}}_0\right\}\mathbf{V}. \tag{19}$$

To include experimentally observed structural and hydrodynamical damping, a diagonal Rayleigh damping term [B] is included. The damping ratio ξ_i is $\xi_i = B_i/(2\sqrt{k_i m_i})$, which means that $B_i = 2\xi_i m_i \omega_i$. The damping ratio is expressed relative to the dry mass of the shell. The hydroelastic modal equation system is integrated in time using the Newmark-beta time integration procedure as defined by Cook et al. (2002) p. 418. This is an implicit method where the unknown at the new time step $n+1$ is found by solving the following equation system,

$$\begin{aligned} \left[\mathrm{K}^{\mathrm{eff}}\right]\{Z\}_{\mathrm{n+1}} = &-\left\{\dot{A}_3\right\}_{\mathrm{n+1}}\mathrm{V} + \left([M] + [\mathrm{A}]_{n+1}\right)\left\{\frac{1}{\beta\Delta \mathrm{t}^2}\{Z\}_{\mathrm{n}} + \frac{1}{\beta\Delta \mathrm{t}}\left\{\dot{\mathrm{Z}}\right\}_{\mathrm{n}} + \left(\frac{1}{2\beta} - 1\right)\left\{\ddot{\mathrm{Z}}\right\}_{\mathrm{n}}\right\} \\ &+ \left[B + \dot{A}\right]_{\mathrm{n+1}}\left\{\frac{\gamma}{\beta\Delta \mathrm{t}}\{\mathrm{Z}\}_{\mathrm{n}} + \left(\frac{\gamma}{\beta} - 1\right)\left\{\dot{\mathrm{Z}}\right\}_{\mathrm{n}} + \Delta \mathrm{t}\left(\frac{\gamma}{2\beta} - 1\right)\left\{\ddot{\mathrm{Z}}\right\}_{\mathrm{n}}\right\}. \end{aligned} \tag{20}$$

The effective stiffness matrix contains contributions from added mass and damping:

$$\left[\mathrm{K}^{\mathrm{eff}}\right] = \frac{1}{\beta\Delta \mathrm{t}^2}\left([\mathrm{M}] + [\mathrm{A}]_{\mathrm{n+1}}\right) + \frac{\gamma}{\beta\Delta \mathrm{t}}\left[B + \dot{\mathrm{A}}\right]_{\mathrm{n+1}} + [\mathrm{K}]. \tag{21}$$

The modal velocity and acceleration vectors are calculated from:

$$\left\{\dot{\mathrm{Z}}\right\}_{\mathrm{n+1}} = \frac{\gamma}{\beta\Delta \mathrm{t}}\left(\{\mathrm{Z}\}_{\mathrm{n+1}} - \{\mathrm{Z}\}_{\mathrm{n}}\right) - \left(\frac{\gamma}{\beta} - 1\right)\left\{\dot{\mathrm{Z}}\right\}_{\mathrm{n}} - \Delta \mathrm{t}\left(\frac{\gamma}{2\beta} - 1\right)\left\{\ddot{\mathrm{Z}}\right\}_{\mathrm{n}}. \tag{22}$$

$$\left\{\ddot{\mathrm{Z}}\right\}_{\mathrm{n+1}} = \frac{1}{\beta\Delta \mathrm{t}^2}\left(\{\mathrm{Z}\}_{\mathrm{n+1}} - \{\mathrm{Z}\}_{\mathrm{n}} - \Delta \mathrm{t}\left\{\dot{\mathrm{Z}}\right\}_{\mathrm{n}}\right) - \left(\frac{1}{2\beta} - 1\right)\left\{\ddot{\mathrm{Z}}\right\}_{\mathrm{n}}. \tag{23}$$

The time derivative of the added mass $\left[\dot{A}\right]$ in Eq. (17) is calculated numerically using the standard second order central difference method $\dot{A} = (A_{n+1} - A_{n-1})/(2\Delta t)$. Furthermore, β and γ are the standard Newmark beta time integration parameters.

Initial conditions are necessary for the integration of Eq. (19) in time. At $t = 0$ the added mass, modal amplitudes and their time derivatives are zero. $\left\{\dot{A}_{i0}\right\}$ is harder to evaluate at $t = 0$ since the time derivative of c is infinite. This limit needs to be treated carefully. For very small values of c, $\dot{A}_{i0}$ can be written as:

$$\dot{A}_{i0} = \rho\int_{-L/2}^{L/2}\Psi_i(x, y = 0)dx\frac{\partial}{\partial t}\int_{-c}^{c}\varphi_0\,(x, y, z; t)\,dy. \tag{24}$$

The time derivative of the last integral is equal to $2\pi RV$. The initial condition for $\dot{A}_{i0}$ is then:

$$\dot{A}_{i0} = \rho 2\pi RV\int_{-L/2}^{L/2}\Psi_i(x, y = 0)dx \text{ for }, t = 0. \tag{25}$$

The hydrodynamical boundary value problem is solved using a 2D strip theory. The strips are directed in the circumferential direction of the shell, and the width of each strip are set equal to the distance between the nodes of

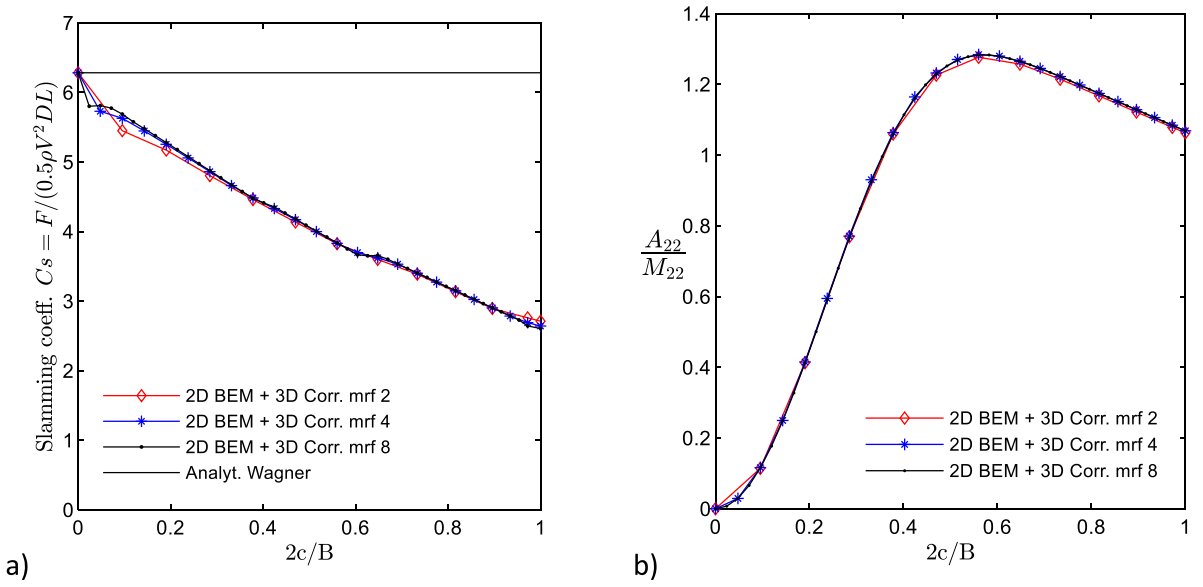

Fig. 12. Convergence test of (a) total slamming force coefficient of the shell and (b) the added mass divided by the structural modal mass of mode 2.

the FE mesh in the axial direction. The hydrodynamical boundary value problem of each strip is solved by using the 2D boundary element method (BEM) described by Abrahamsen (2011). Boundary elements are distributed along the edge of a rectangular BEM domain. The velocity potential is set to zero along the free surface and equal to a wall condition on the three lower sides. Sufficient domain size and number of elements are identified through a dedicated convergence study. The effect of 3D flow are accounted for by multiplying the velocity potential at every point along the strip with a factor *J(y,k)*. This factor is the ratio of the added mass of the heaving strip on a plate with finite width, divided by the 2D added mass of that strip. The function *J(y,k)* is taken from Fig. 9 of Meyerhoff (1970). This function is derived for a rigid heaving plate. In this work the same function is used on the potential flow calculation for all modes included in the solution. The added mass for each strip is calculated for each mode of motion for all the different submergences of the shell prior to solving the coupled problem in Eq. (19). The validity of the 2D strip theory is studied numerically in Fig. 13 where shell responses are calculated based on both 2D strip theory and 3D potential flow theory.

Fig. 12 shows a convergence study of the 2D BEM solver. Plot (a) shows the slamming coefficient for different values of nondimensional *c* and (b) shows the added mass coefficient of governing mode for the thick model elastic shell as a function of wetting, *2c/B*. The convergence study was carried out with 6 boundary elements per structural shell element to obtain reasonable convergence for the slamming coefficient.

To ensure that the time step also resolved the structural response a second parameter N_{crit} is defined, which is the number of timesteps per lowest dry natural period of the shell. All simulations carried out in the later sections of this paper, except the plots discussing damping and convergence in Fig. 13, are carried out with the following standard numerical settings: (1) The shell element mesh with 4 finite elements between each bolt ($mrf = 4$) is applied. (2) The time step parameter N_{crit} is set to $N_{crit} = 200$ timesteps per lowest natural period of the modal expansion. (3) The number of modes in the modal expansion are set to $N_m = 27$. (4) The Newmark time integration constants are set to; $\beta = 0.25$ and $\gamma = 0.5$. (5) The Rayleigh damping is set to 1.5% for all modes, which is a value discussed in the following text.

Fig. 13(a) shows time history of the hoop bending moment at pt 4 for the thick elastic shell for drop test 9 with impact velocity of 12.19 m/s. The difference between the green and the blue curve shows the effect of a Rayleigh damping of 1.5% on all modes. The very important first peak of the bending moment is not significantly affected by the damping, while the later peaks are damped like the experimental curve.

To document the structural damping, the shell was hit with a hammer at the location of the centre accelerometer (pt. 2–2) while in air. Fig. 13(b) shows the free decay after the hit. The dry vibrations show a decay of about 0.7% for the lowest mode of motion.

Fig. 13(c) shows the sensitivity of the number of elements between the bolts, the mesh refinement factor *mrf*, on the time history of the hoop bending moment at the centre of the shell, pt 4. From a practical engineering perspective, the most important time instant is that of maximum bending moment. The maximum hoop bending moment at pt. 4 for the 3 meshes, mrf 2, 4 and 8 reads: 11 176, 12 162, 12 619 kNm/m. Ideally, the sensitivity of the mesh on the solution would be zero. Here the maximum bending moment for mrf 2 is 11% lower than the finest mesh of mrf 8. The mrf 4 mesh, which is the mesh used in all the latter simulations is 3.6% lower than the finest mesh of mrf 8. The indicated level of error should be accounted for when comparing experimental and theoretical results in the following section. Furthermore, Fig. 13(d)

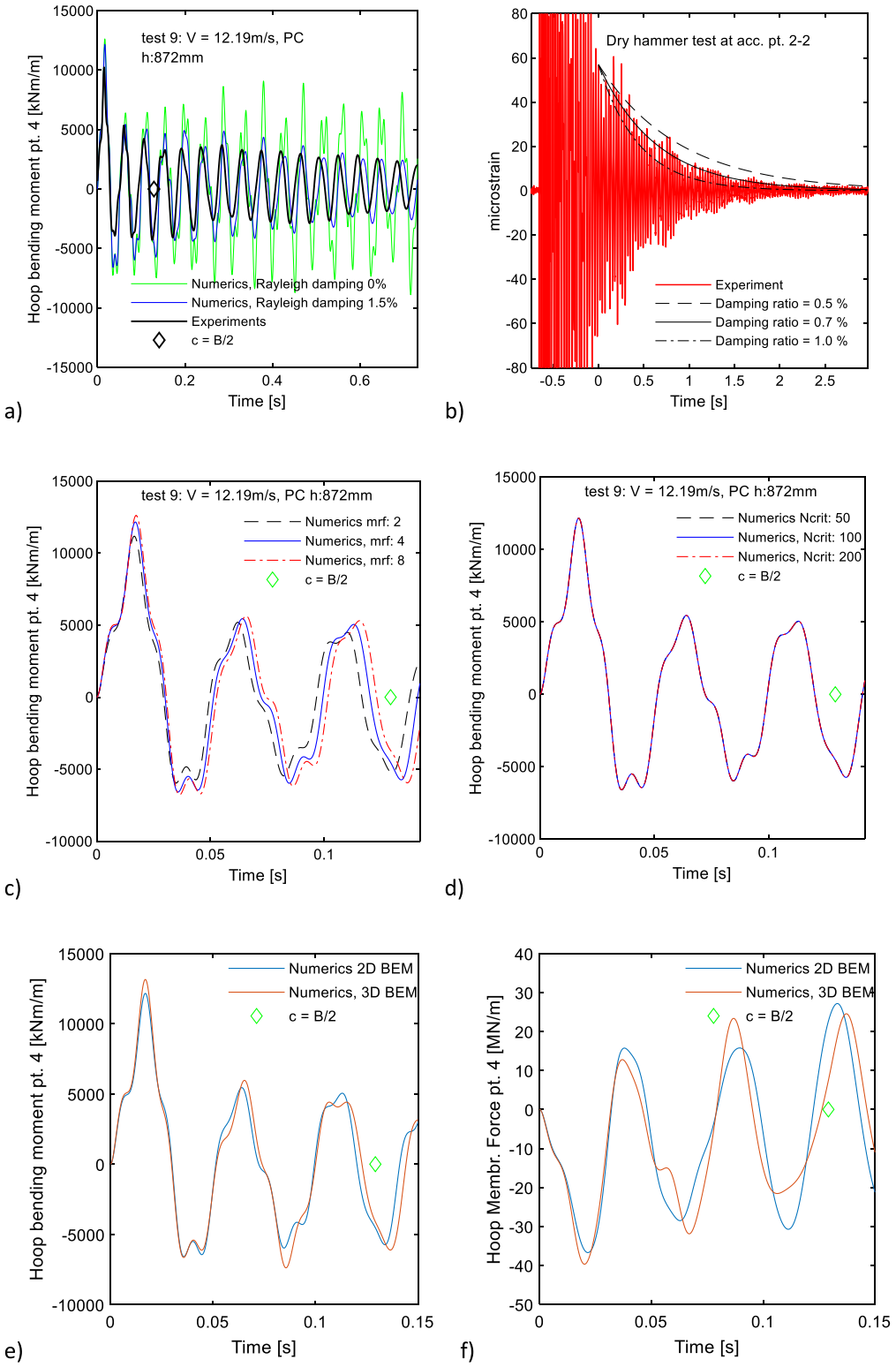

Fig. 13. (a) Effect of Rayleigh damping of 1.5%, for all modes, on bending moment time series at the front of the shell (pt. 4). Plot (b) shows the free vibrations of the shell and an estimate of the structural damping of 0.7%. Plot (c) shows a convergence study when refining the FEA and BE meshes by a factor of 2, 4 and 8 and plot (d) shows a convergence study when refining the time step. (For interpretation of the references to colour in this figure legend, the reader is referred to the web version of this article.)

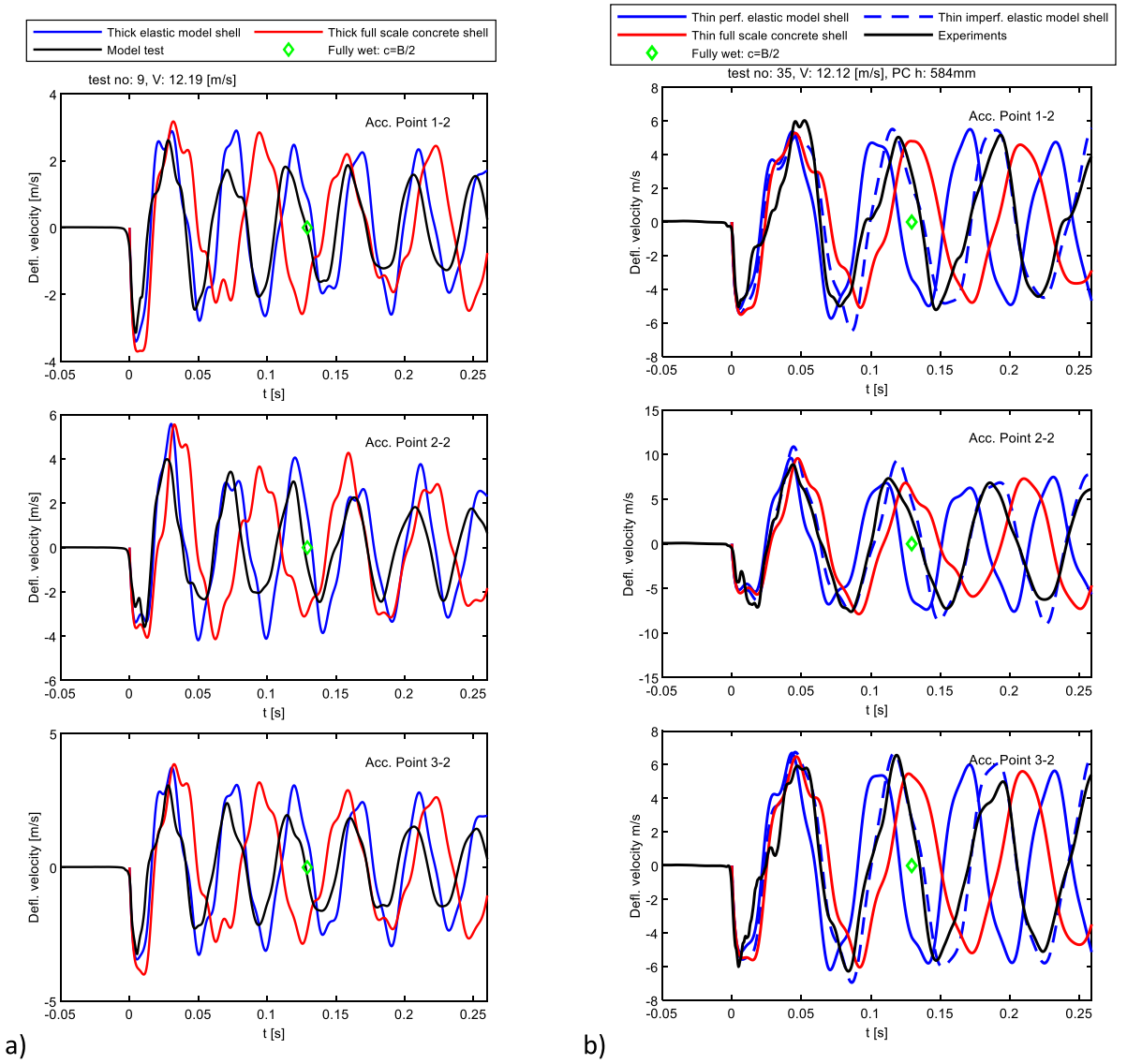

Fig. 14. Comparison of measured and calculated deflection velocity for acceleration measurement points (1,2), (2,2), (3,2) from experiments and from numerical model of the Froude scaled elastic model shells and full-scale concrete shells. Plot (a) shows the results for the thick shells, while (b) shows the results for the thin shells. (For interpretation of the references to colour in this figure legend, the reader is referred to the web version of this article.)

shows the effect of refining the time step through the N_{crit} parameter. The effect of temporal refinement is negligible compared reported effect of spatial refinement in Fig. 13c.

Fig. 13(e) and (f) show hoop bending moment and membrane forces at pt. 4, using *mrf* equal to 4, using the 2D strip theory including the 3D corrections and full 3D potential flow theory using Wamit (Wamit, 2020) to solve the hydrodynamic problem. This numerical calculations show that the extreme bending moment and membrane force max|M|, max|N| are 8% higher when based on 3D Wamit calculations than when based on the 2D strip theory calculation including 3D correction.

5. Comparison of experiments and theory

The results from the numerical method are compared to the experimental measurements. Fig. 14 shows the deflection velocity at the locations of the 3 accelerometers along the front of the shell 1–2, 2–2 and 3–2. Plot (a) shows the results for the thick elastic shell for test 9 with impact velocity of 12.19 m/s, while plot (b) shows the results for the thin elastic shell for test 35 with impact velocity of 12.12 m/s. For both plot (a) and (b) the experimental results (black curve) are calculated

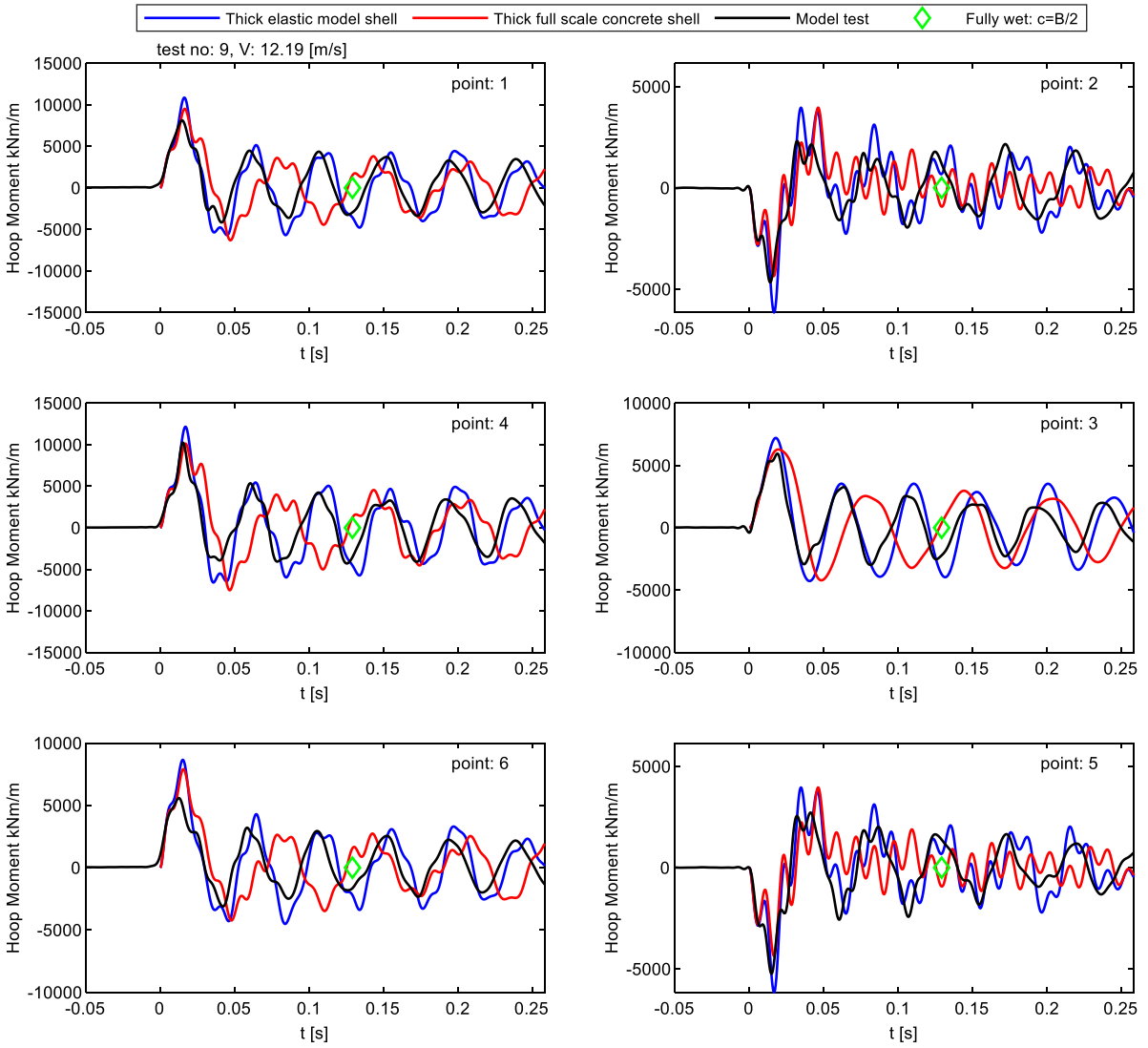

Fig. 15. Comparison of measured and calculated bending moments in the hoop direction for the 6 measurement points on the thick elastic shell for drop test 9 with impact velocity of 12.19 m/s.

by integration of the difference between the measured acceleration on the plate and on the test-rig frame just behind the measurement point. For the thin shell in plot (b) there are two blue curves, the full blue line indicates the hydroelastic solution with a perfectly circular shell, while the dashed blue curve shows the solution when the imperfection of the thin elastic shell, shown in Fig. 4(a), is accounted for in the structural FEA modelling and 2D BEM calculations.

For the thick elastic shell in Fig. 14 plot (a) the accuracy of the hydroelastic method is assessed by studying the difference between the blue and the black lines. For the impact and the initial oscillation, amplitudes and oscillation periods agree well. In subsequent oscillations some amplitudes are slightly higher, and there is a tendency that the period of oscillation is slightly larger for the hydroelastic calculations than for the measurements. For the thin elastic shell in plot (b) the accuracy of the hydroelastic method can be assessed by studying the difference between the dotted blue curve, which accounts for the imperfection of the shell, and the black curve. For the impact and the initial oscillation, amplitudes and oscillation periods agree well. In subsequent oscillations the comparison shows that both the amplitudes and the period of oscillation are slightly more accurate for the thin than for the thick elastic shell.

The measured hoop bending moments in the thick shell for the six measurement points are plotted in Fig. 15. These time series were measured during test 9 with impact velocity of 12.19 m/s. Fig. 16 shows the thin shell during test 35 with impact velocity of 12.12 m/s. The maximum bending moments are overpredicted for the thick elastic plate while the thin elastic plate the simulations are more accurate.

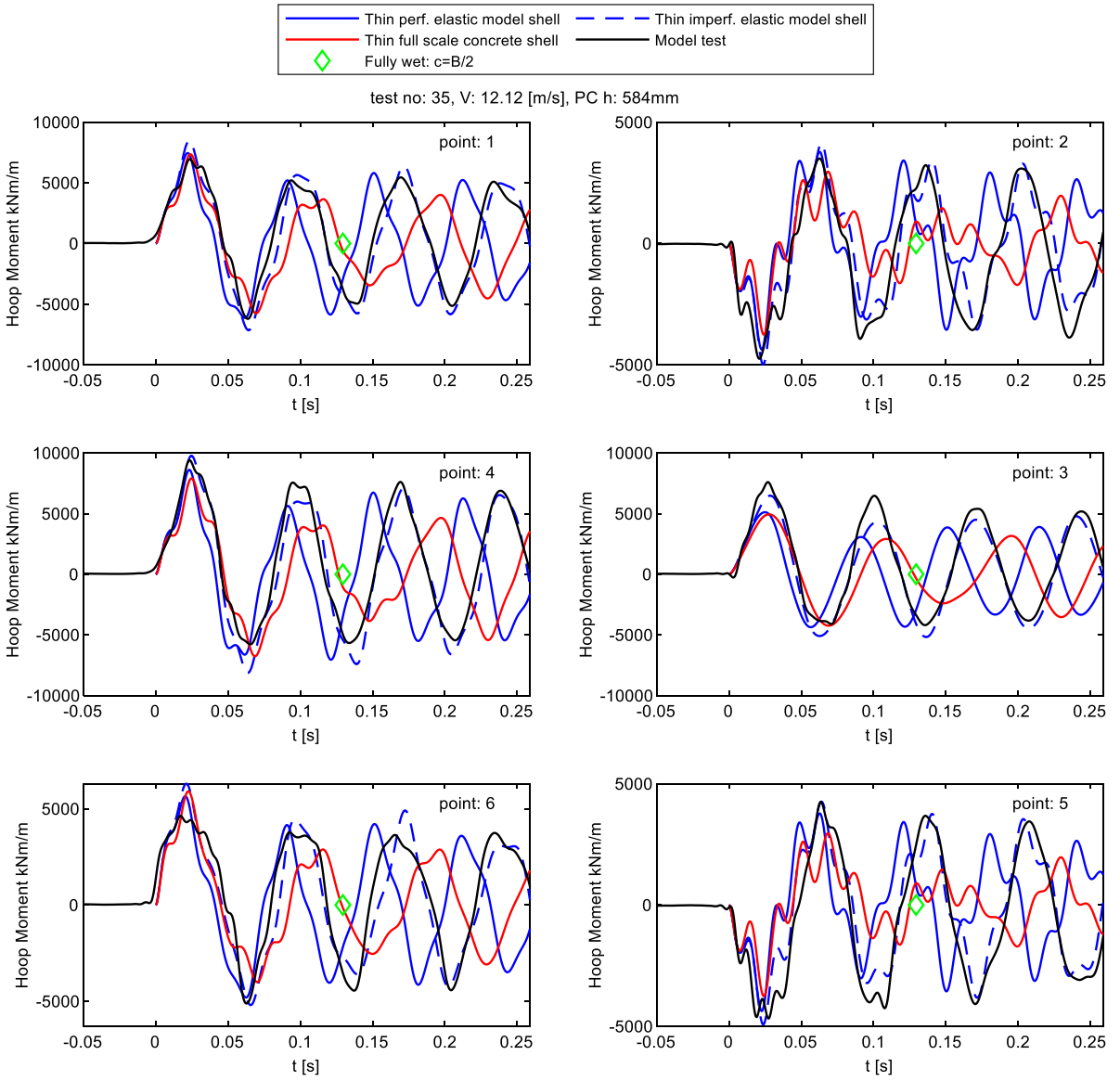

Fig. 16. Comparison of measured and calculated bending moments in the hoop direction for the 6 measurement points on the thin elastic shell for drop test 35 with impact velocity of 12.12 m/s. (For interpretation of the references to colour in this figure legend, the reader is referred to the web version of this article.)

The difference between the full blue and the dashed blue curves in Figs. 14 plot (b) and 16 shows the effect of the imperfection of the thin shell. The most noticeable difference is that the period of oscillation is considerably more accurate when the imperfection is accounted for. The extreme responses are not significantly affected by the imperfection.

Figs. 17 and 18 shows the hoop membrane force of the shell at the measurement points 1 to 6 for the same impact. For both the thick and the thin shell the largest membrane force occurs during the first half-period of oscillation.

The comparisons of the time series show that the numerical solution predicts the deformation velocity and membrane forces of the shell accurately. The bending moment of the thick shell is overpredicted but is more accurate for the thin shell.

6. Extreme response as a function of impact velocity

In this section the numerical method was used to study the extreme response of the shells for a wide range of impact velocities spanning from 5 to 25 m/s. In this work the extreme response is defined as the maximum of the absolute value

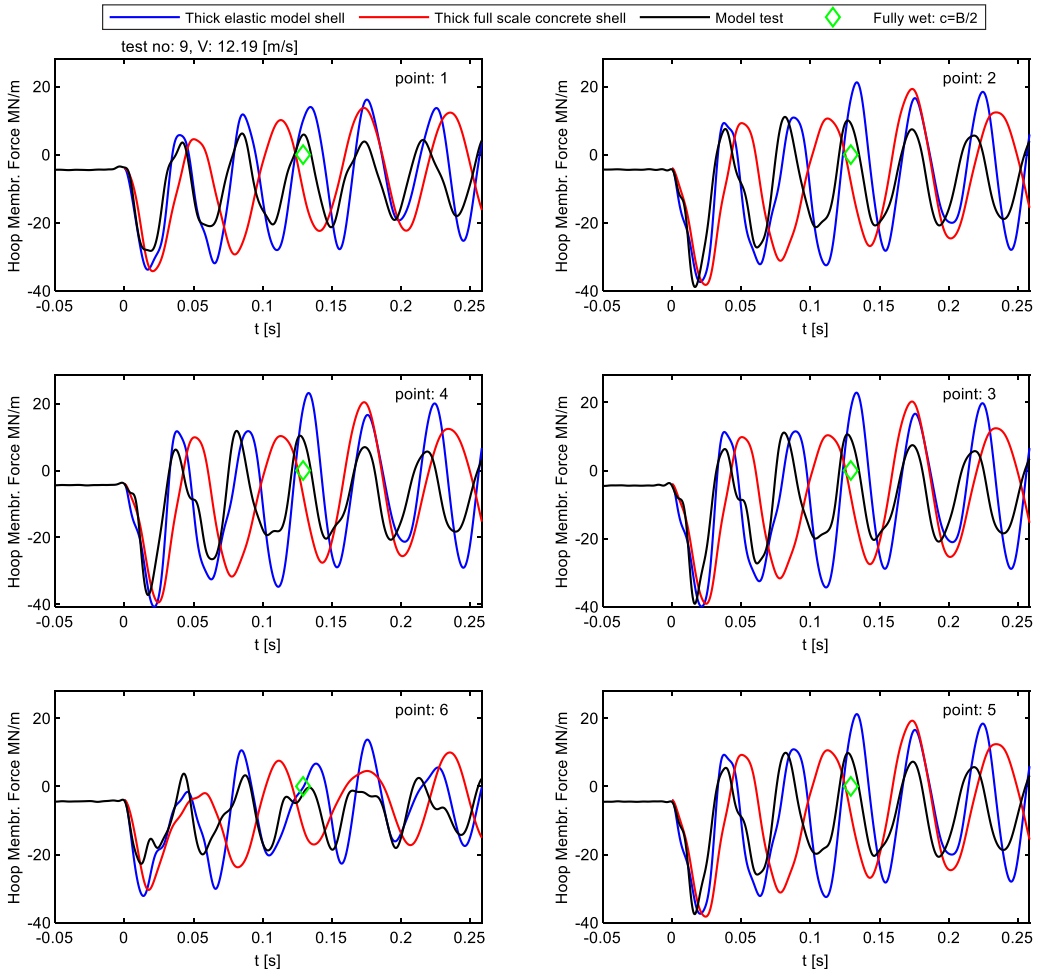

Fig. 17. Comparison of measured and calculated membrane force in the hoop direction for the 6 measurement points on the thick elastic shell for drop test 9 with impact velocity of 12.19 m/s.

of the response time series. The main motivation was to study the effect of hydroelasticity on extreme responses through comparisons of static and hydroelastic calculation results.

Figs. 19 and 20 shows the extreme bending moments as a function of impact velocity for the thick and the thin shell. Figs. 21 and 22 shows the corresponding extreme hoop membrane forces. Hydroelastic analysis of the model shell are shown as the blue curve, hydroelastic analysis of the full-scale concrete shell as the dashed blue curve, static analysis of the elastic model shell as the red curve and static analysis of the full-scale concrete shell as the dashed red curve.

Fig. 19 show that the hydroelastic solution for the thick shell overestimates the extreme bending moments for all drop heights. For the thin shell, Fig. 20, an extra green curve was plotted. This curve shows the hydroelastic solution when the imperfection of the shell is accounted for in the analysis. The imperfection is seen to cause larger extreme bending moments and can explain some of the discrepancies between the measurements and the calculations with a perfectly circular shell. Furthermore, the calculations of extreme bending moments are more accurate for the thin shell than for the thick shell for the whole range of impact velocities.

The effect of hydroelasticity on the extreme bending moments is the difference between hydroelastic solutions seen as the blue curves and the corresponding red curves indicating the static solutions. For all points and both shells a critical impact velocity can be identified for which the static solution crosses the hydroelastic solution. This intersection point varies across the measurement points, for the two thicknesses, and between full-scale and model-scale.

Figs. 21 and 22 shows the extreme dynamic hoop membrane force. This membrane force was calculated as in Eq. (6), but without the static contribution from the prestressing of the concrete. The figures show the extreme hoop membrane force for all 6 measurement points as a function of impact velocity for the thick and the thin shells. The description of the different curves follows from Figs. 19 and 20. The plots show that the extreme membrane forces from the hydroelastic method are generally more accurate for extreme membrane forces than for the extreme bending moments. Furthermore,

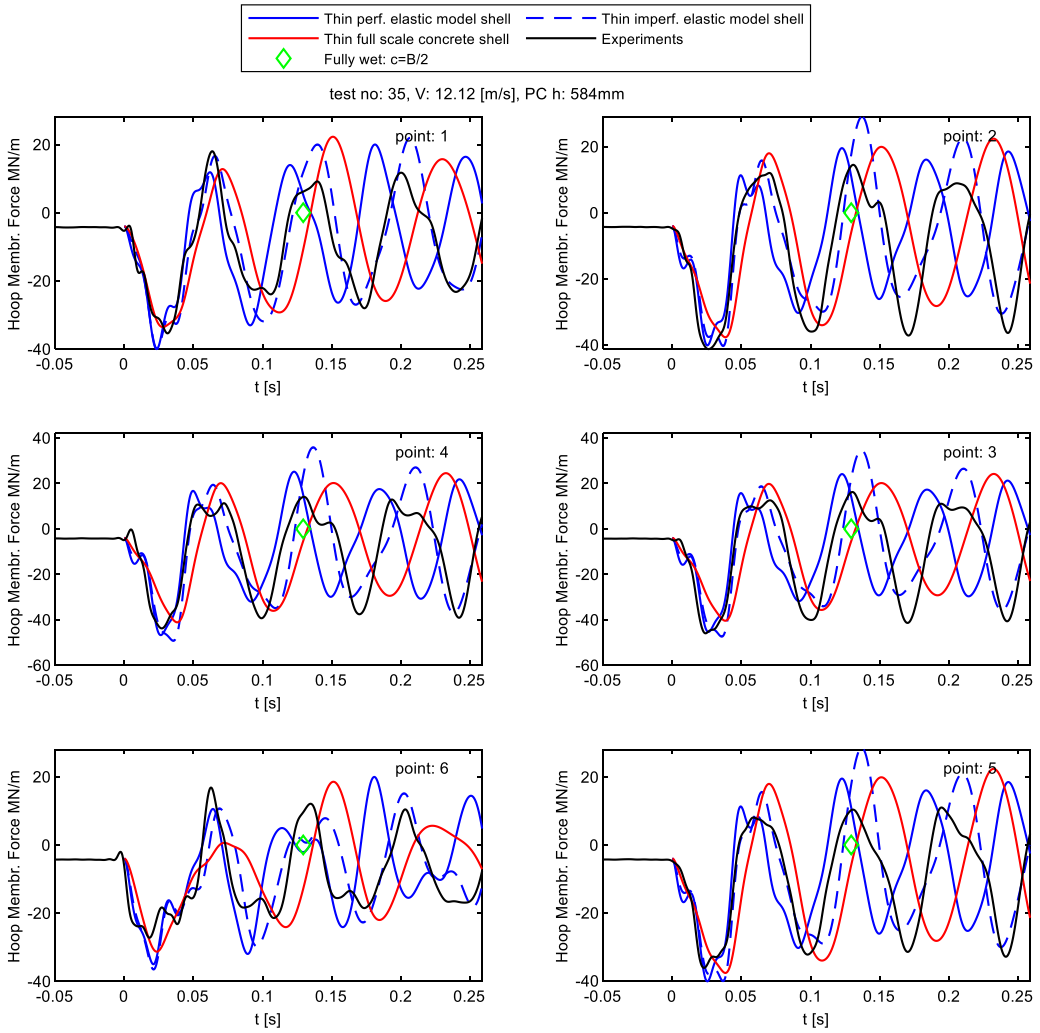

Fig. 18. Comparison of measured and calculated membrane force in the hoop direction for the 6 measurement points on the thin elastic shell for drop test 35 with impact velocity of 12.12 m/s.

the plots show that the extreme hoop membrane force is less sensitive to imperfections than the extreme hoop bending moments. Also, the difference between the extreme membrane force from hydroelastic calculations are much larger than for the static calculations for the whole range of impact velocities calculated.

The difference between the numerically calculated and measured extreme hoop bending moment and membrane force were quantified. The differences are calculated based on the data in Figs. 19–22. The average deviation was estimated for four drop tests each at a different drop height. The deviation for each drop height were estimated as $(num - meas)/meas * 100$, were *num* and *meas* denotes the numerical and experimental value of the extreme bending moment or membrane force. These average deviations of extreme hoop bending moment and extreme membrane force compared to experiments are listed in Table 3, and show that the numerical solution overpredicts the extreme bending moments between 17 and 24% for measurement point 1 to 5 for the thick elastic shell. However, the corresponding extreme membrane force is far more accurate with a deviation from −7 to 10%. The experimental error sources discussed in Section 3 is; (1) repetition errors with a standard deviation less than 3%, (2) strain gauge errors expected to be less than 2% and, (3) uncertainty of the Young's modulus which is expected to be less than 5%. The experimental uncertainties are not sufficient to explain the difference between calculated and measured extreme hoop bending moments for the thick elastic shell. Furthermore, the numerical errors which were investigated at the end of Section 4, mesh refinement which increases of the extreme hoop bending moment of 3.6% and full 3D potential flow calculations which increased the hoop bending moments by 8%, Both results in event higher calculated bending moments which both suggests that more accurate analysis would increase the discrepancy between theory and experiment not reduce it. Hence, a proper explanation of the overestimation of the extreme hoop bending moments for the thick elastic plate were not identified.

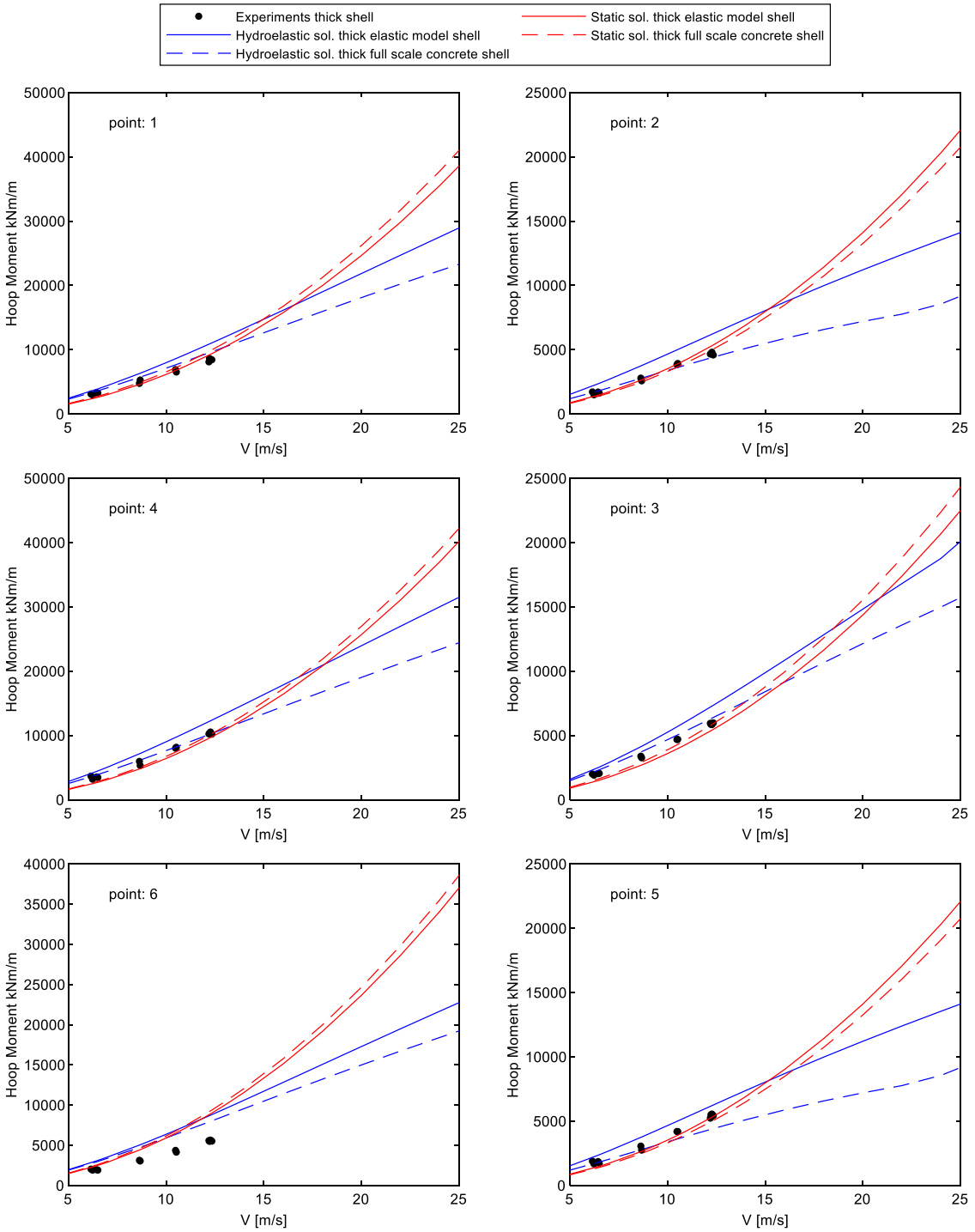

Fig. 19. The extreme hoop bending moments as a function of impact velocity for the thick elastic shell. (For interpretation of the references to colour in this figure legend, the reader is referred to the web version of this article.)

For measurement point 6 the extreme hoop bending moment is overpredicted by 37% and the extreme membrane force the overprediction is 26%. This is far larger discrepancy than for the other measurement points on the thick elastic shell. Measurement point 6 on the thick elastic section is likely defect since the measured bending moments and membrane forces were much lower than at point 1 on the same elastic shell. Although point 1 and 6 are not located completely symmetrically, the strains are not expected to be that different. This is supported by the measurements on the thin elastic

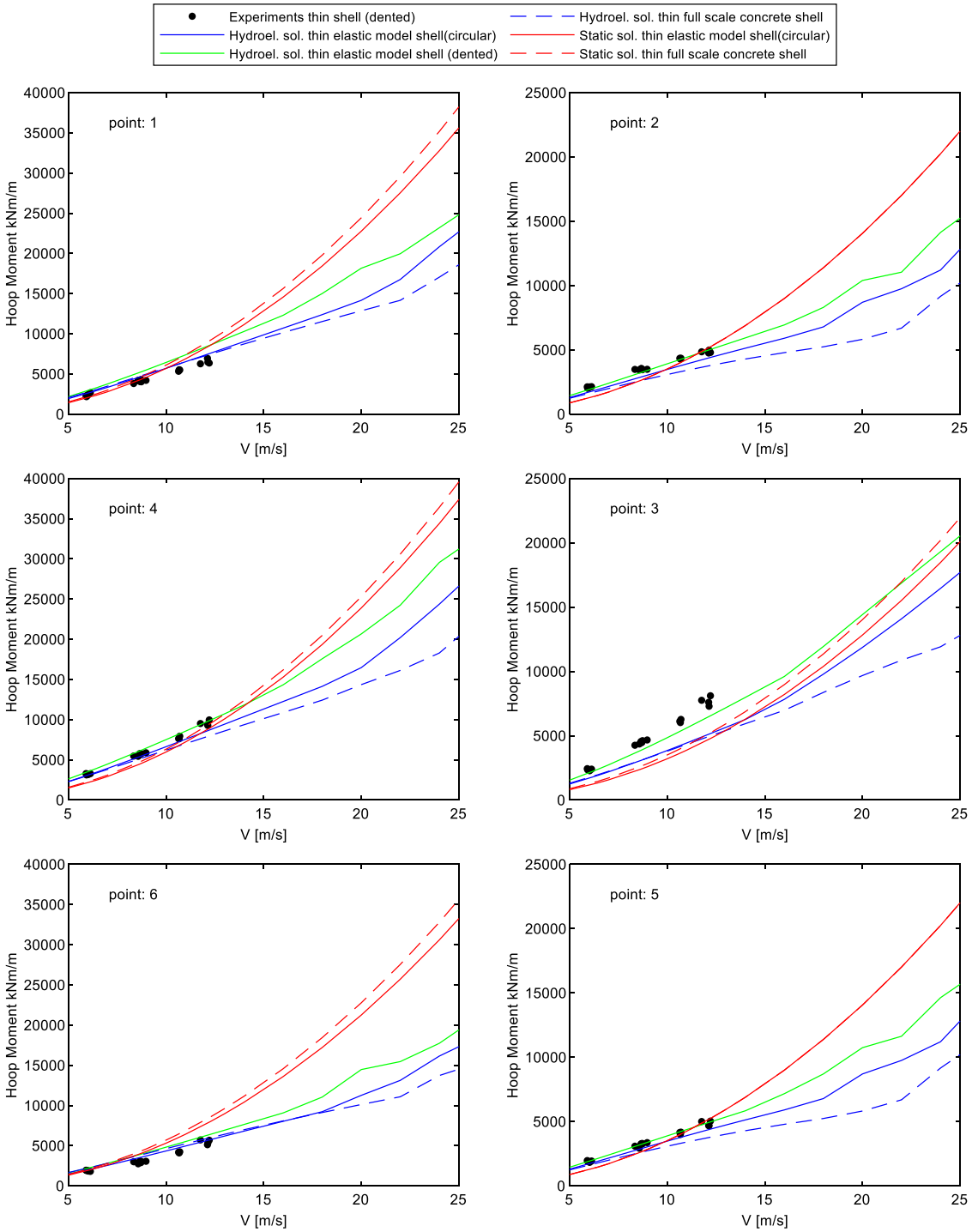

Fig. 20. The extreme hoop bending moments as a function of impact velocity for the thin elastic shell. (For interpretation of the references to colour in this figure legend, the reader is referred to the web version of this article.)

section and the hydroelastic calculations for both the thin and the thick elastic shells. A physical cause of this defect was not identified.

For the thin elastic shell average deviations were calculated using the dented shell geometry. For the thin elastic shell, the error of the extreme bending moments spans from −22 to 15% for all measurement points while the extreme membrane force deviates between −15 to 16% in average for the four drop heights. In contrast to the thick elastic shell,

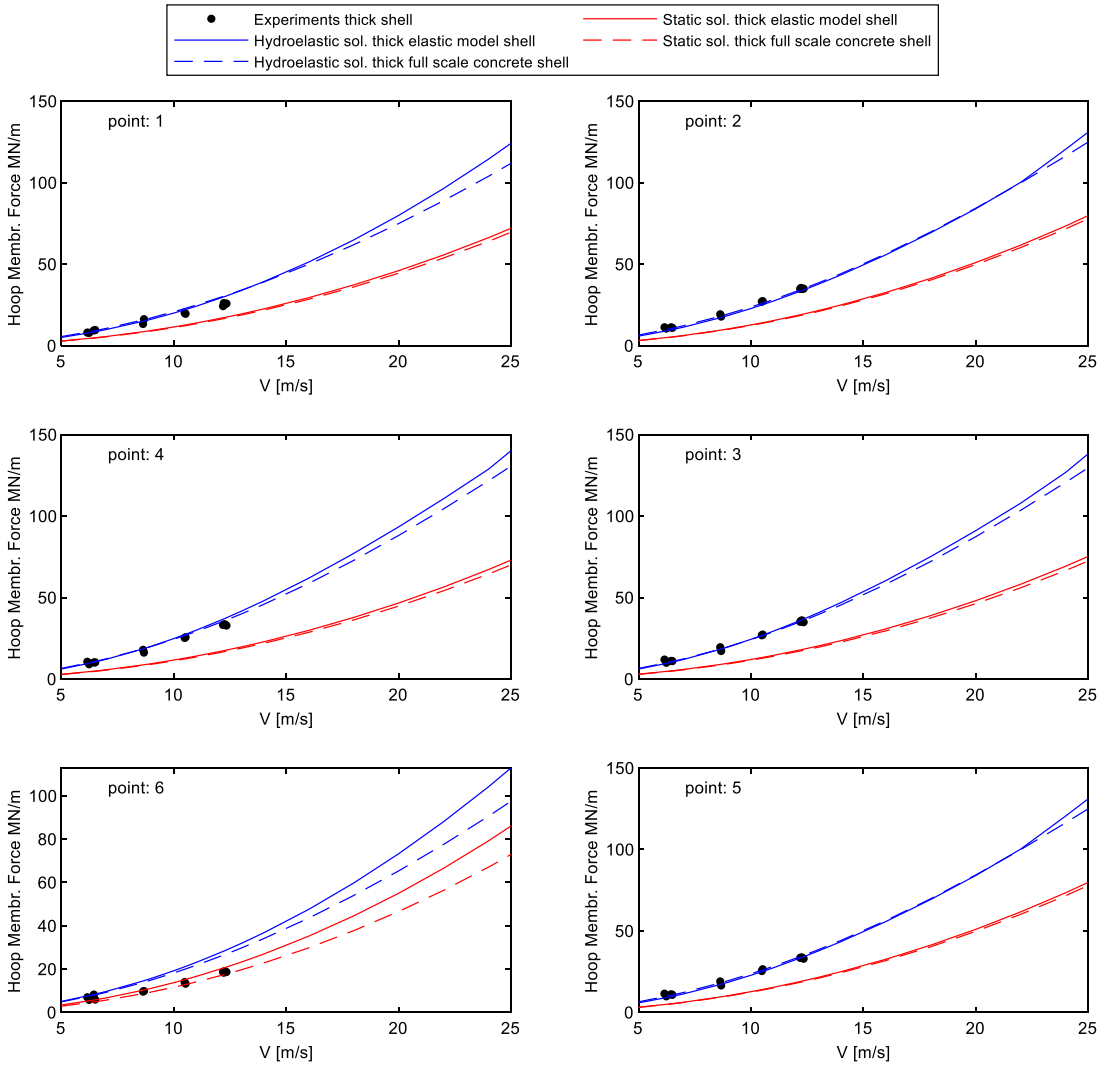

Fig. 21. The extreme dynamic hoop membrane force as a function of impact velocity for the thick elastic shell. (For interpretation of the references to colour in this figure legend, the reader is referred to the web version of this article.)

the numerical calculations for the thin elastic shell does not systematically overestimate the extreme bending moments. The largest deviations are found for the extreme hoop bending moments measured at point 1 and 6, where the numerical method overestimates the extreme bending moments by 22 and 20%.

7. Accuracy of Froude scaled elastic shells

The presented timeseries of response suggests that a limited number of modes contributes to the response of the shell. The two most important modes are shown in Fig. 23. The upper row of plots shows the thin model shell, the thin concrete shell, the thick model shell, and the thick concrete shell for the most important mode for deflections, shell bending moments and shell membrane forces. It governs the radial displacement along the front of the shell, and it dominates the bending moments at all strain measurement locations. Together with the mode on the second row it also governs the hoop membrane response of the shell. The mode on the second row dominates the radial displacement of the shell at the left and right sides. In the case that the shells were perfectly scaled, the mode shapes and eigenfrequencies of the model and the full-scale concrete shells would be identical. Fig. 23 shows to what extent this is the case and hence shows the shell scaling error. The upper row of plots shows that the dominant mode is more accurately scaled for the thin shell than for the thick shell. The calculated dry natural frequencies are given above each plot. The experimental dry natural frequencies were documented through impact tests with a hammer, hitting the shells at their centres. The experimental dry natural frequencies were 35.7 Hz for the thick elastic shell, which is a bit higher than the calculated

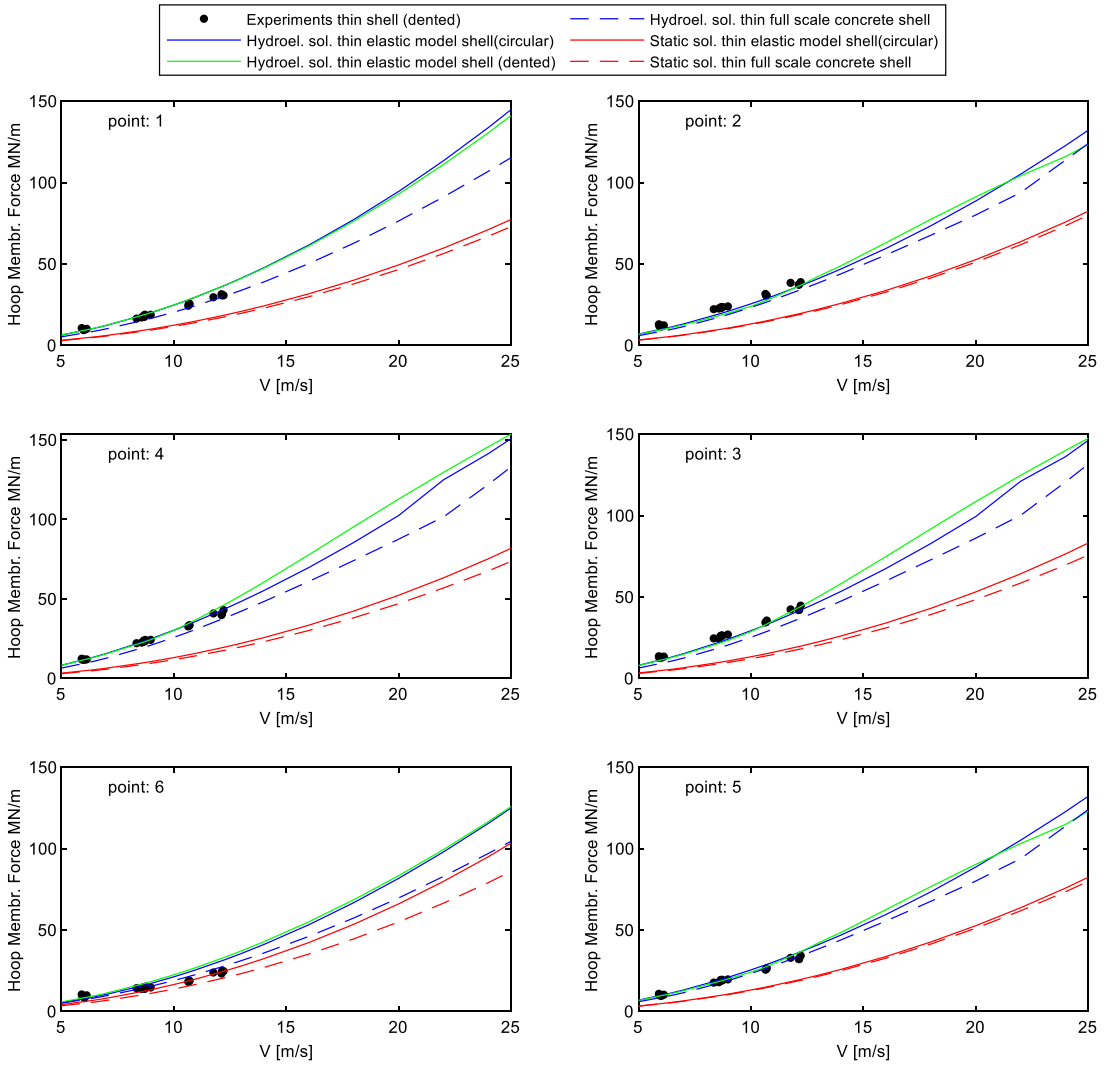

Fig. 22. The extreme dynamic hoop membrane force as a function of impact velocity for the thin elastic shell. (For interpretation of the references to colour in this figure legend, the reader is referred to the web version of this article.)

Table 3
The average deviation of extreme hoop bending moments and membrane forces between numerical calculations and measurements. The average deviation of the four studied drop heights is presented for the thin and the thick elastic shell.

Deviations: Numerics - Experiments						
Meas. point:	1	2	3	4	5	6
Unit	%	%	%	%	%	%
Thick shell						
max|M|	−21	−24	−18	−17	−17	−37
max|N|	−7	10	4	−5	8	−26
Thin shell						
max|M|	−22	2	15	−7	−2	−20
max|N|	−8	16	8	−4	−3	−15

natural frequency of 33.6 Hz. For the thin elastic shell, the experimental dry natural frequency was 24.9 Hz for the thin elastic shell, which is a bit lower than the natural frequency of the perfectly circular shell, 25.4 Hz and a bit higher than the natural frequency for the imperfect shell which had a natural frequency of 23.9 Hz.

The effect of the shell scaling error on the deflection velocities is the difference between the blue and red curves in Fig. 14. The effect of the shell scaling error on the timeseries of the hoop bending moments and membrane forces can be

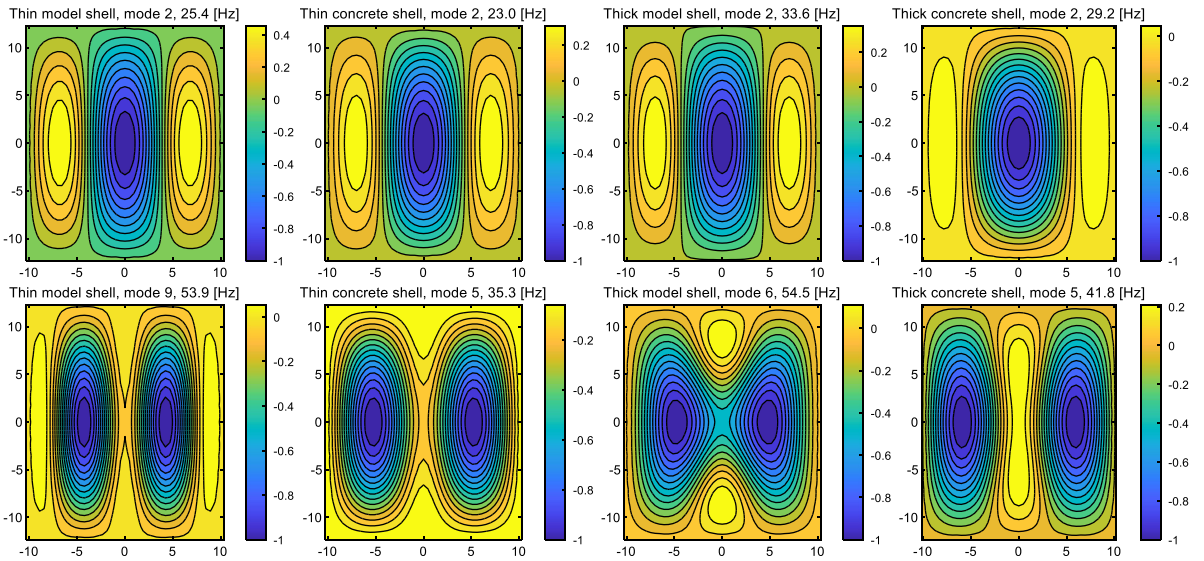

Fig. 23. Radial displacement of governing shell response modes for the thin and thick elastic model shells and full-scale concrete shells. The upper row of plots shows the most important mode with respect to deflection along the centreline and bending moments in the whole shell. The second row of plots shows the mode governing the radial displacement on the left/ right side of the shell and this mode also significantly contributes to the hoop membrane forces in the shell.

found by studying Figs. 15–18. Both the thin and the thick shells have a period of oscillation which is larger in full-scale than model scale. The effect of shell scaling errors on the extreme shell responses are shown in Figs. 19–22.

The calculated extreme hoop bending moment and membrane force for the Froude scaled elastic shells are higher than the hoop bending moment and membrane force for the full-scale concrete shells. The overprediction increases with the impact velocity V. For the extreme hoop bending moment of the thick shell, this overprediction is 18% and 28% for impact velocity of 10 and 24 m/s close to the shell centre (pt. 4). For the thin shell this overprediction is 8% and 33% for impact velocities of 10 and 24 m/s. The extreme hoop membrane force calculated for the Froude scaled elastic shell is more accurate than the extreme hoop bending moments. The extreme hoop membrane force close to the centre point calculated for the thick Froude scaled elastic shell is 2% and 6% higher than for the thick full-scale concrete shell at impact velocities of 10 and 24 m/s. For the thin shell this overestimation of extreme hoop membrane force was 17% and 16% for the impact velocities of 10 and 24 m/s respectively.

8. Dynamic amplification factors

The extreme structural responses of the shell are most important in the design. A relevant measure on the effect of hydroelasticity is hence the ratio between the extreme response when hydroelasticity is accounted for and the extreme response from a static analysis. In this section dynamic amplification factors DAFs for the deflections w, hoop bending moments M, and hoop membrane forces N are calculated for the measurement points close to the centre of the shell. DAF is defined as the maximum absolute value of the response (w, M, N) from the hydroelastic calculations divided by the maximum absolute value of the response from the static analysis. Fig. 24(a) shows the DAF of the shell displacement near the shell centre (pt 2–2), while (b) shows the DAF of the hoop bending moment near the shell centre (pt. 4) and (c) shows the DAF of the hoop membrane force at the centre point (pt.4). The x axis in all three plots is the load duration T_d divided by the dry natural period of the governing mode (mode 2) denoted T_n. These natural frequencies are shown in the top row of plots in Fig. 23. T_d was defined as the time from the start of the impact to the time when the section was fully wet, estimated from Eq. (18). DAFs are plotted for the thin model shell, thick model shell, thin concrete shell, and thick concrete shell.

The DAFs were derived for impact velocities from 4 to 40 m/s, which is a wide range of velocities. Relevant impact speeds of design critical slamming waves governing the design in the North Sea spans from 10 to 24 m/s. This range of impact velocities are indicated in the plots. Where (o) indicates 10 m/s and (*) indicates 24 m/s. Table 4 shows the range of DAFs relevant for the different structural responses close to the centre of the plate.

The magnitude of the DAF strongly depends on which response which is considered. The lowest DAFs are seen for the hoop bending moment for both the thin and the thick plate ranging from 0.5 to 1.13. Then follows the displacement ranging from 0.73 to 1.38 and the hoop membrane force ranging from 1.8 to 2.18.

None of the DAFs for the response of the concrete shell approached 1 for large values of load duration. This is contrary to the work by Faltinsen (1999) who studied the impact of a stiffened plated steel/aluminium wedge on a flat free surface. In

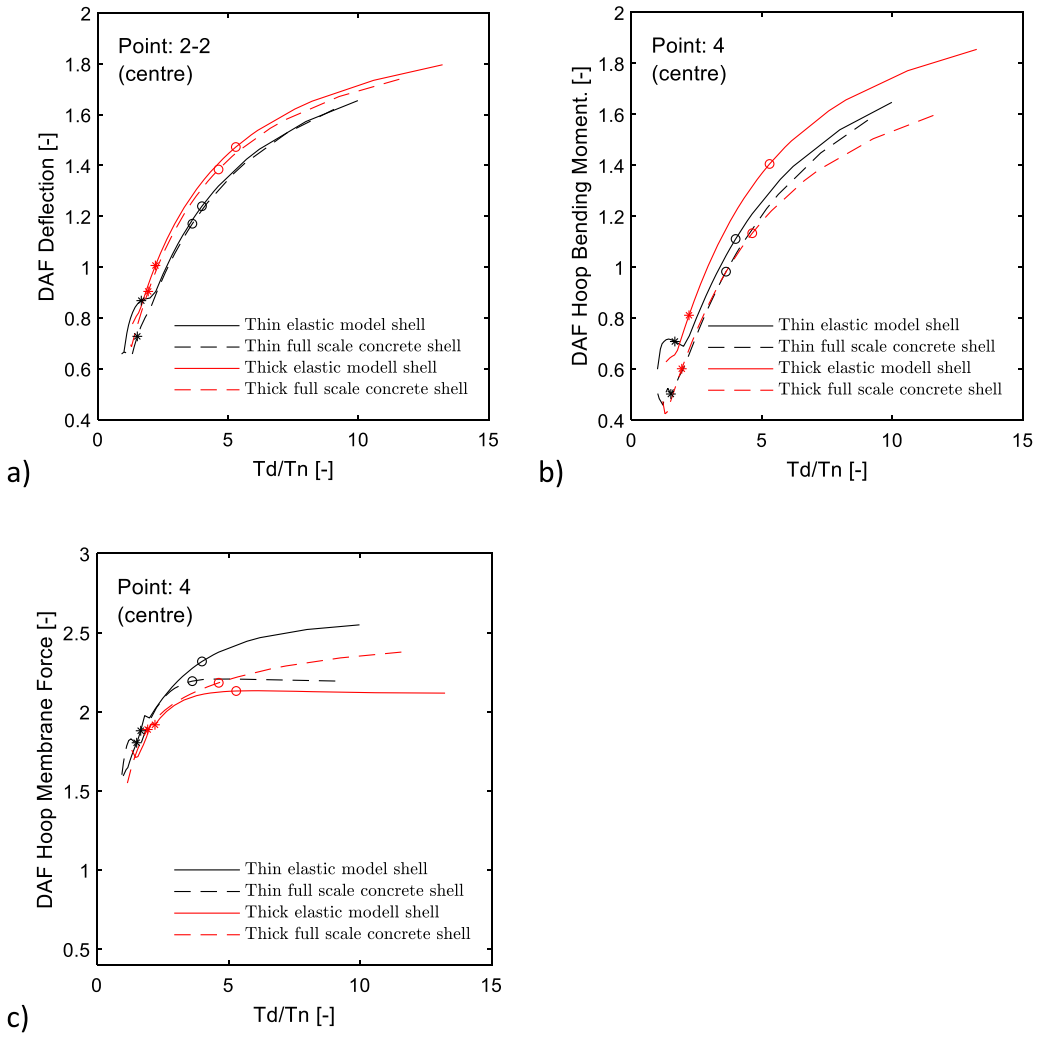

Fig. 24. Dynamic amplification factors versus load duration-to-governing natural period ratio T_d/T_n for (a) the deflection at the centre (pt 2–2), (b) the hoop bending moment at the centre (pt. 4) and (c) the membrane force at the centre (pt. 4). The impact velocity of 10 m/s and 24 m/s are indicated by circles (o) and stars (*) respectively.

Table 4
Relevant range of dynamic amplification factors (DAFs) for deflection, hoop bending moment and hoop membrane force for points close to the centre of the plate and impact velocities ranging from 10 to 24 m/s.

DAF (centre)	Deflection (pt. 2-2)		Hoop bending moment (pt. 4)		Hoop membrane force (pt. 4)	
Shell	24 m/s	10 m/s	24 m/s	10 m/s	24 m/s	10 m/s
Thin concrete	0.73	1.17	0.5	0.98	1.8	2.19
Thick concrete	0.90	1.38	0.6	1.13	1.89	2.18

Faltinsen (1999) the DAF for the strains approach 1 for long load durations. A considerable difference between (Faltinsen, 1999) and the present case is that the rise time of the modal loads for the wedge is finite while it is mathematically zero in the present case. Standard textbooks on structural dynamics often show plots of DAFs of single degree mass spring system exposed to transient loads. See for instance Clough and Penzien (1975) page 94. For a triangular load with zero rise time, which is relevant for the concrete shells studied herein, the DAF goes to 2 for large values of the load duration.

9. Hydrodynamic load modifications due to structural vibration

Fig. 25 shows the deflection near the shell centre (i.e. pt. 2–2). Plot (a) shows the deflection for the thick shell and (b) shows the deflection for the thin shell as a function of time. The deflections are plotted for relevant impact speeds of

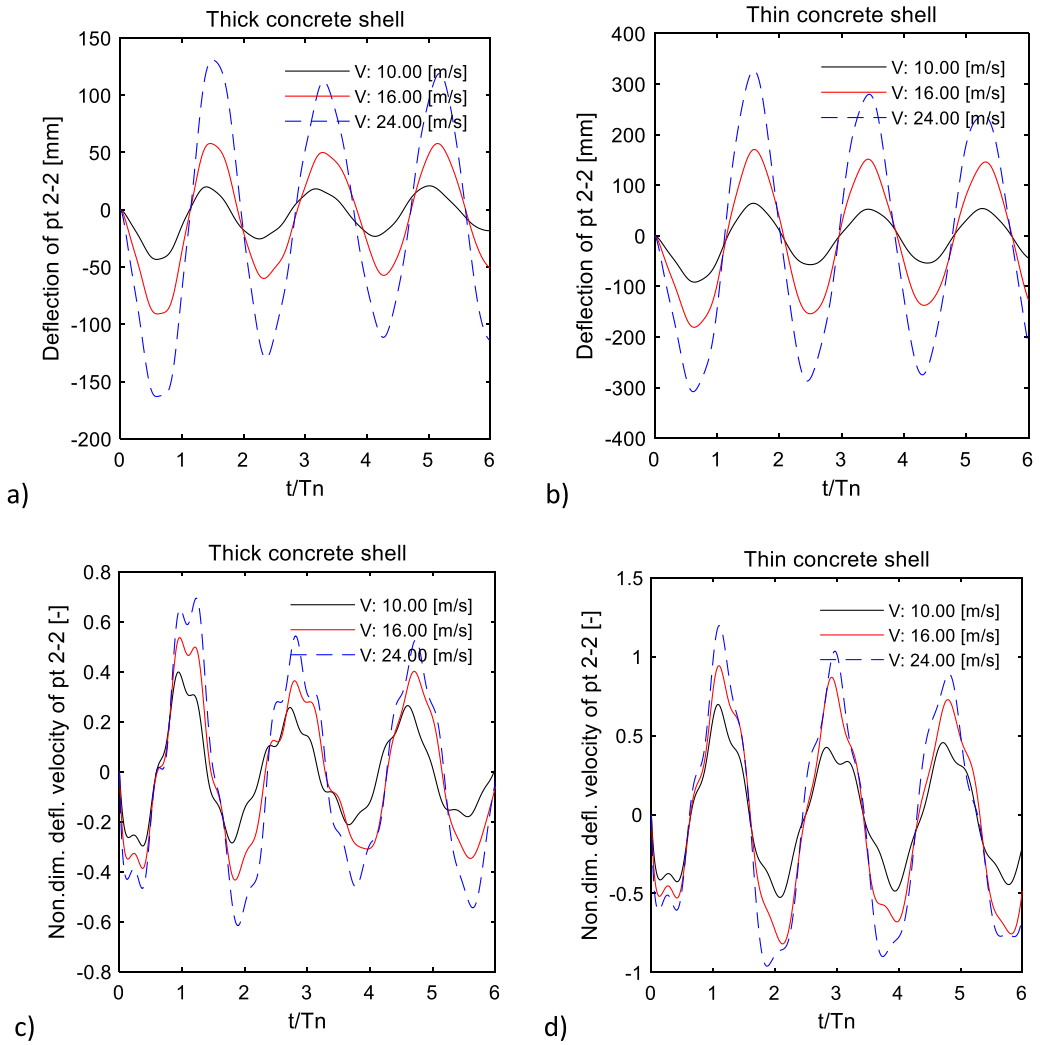

Fig. 25. Plot (a) and (b) shows the deflection near the centre of the shell (pt. 2–2) for the thick and the thin full-scale concrete shells for three impact velocities. Tn is the dry natural period of the governing mode of response (mode 2). Plot (c) and (d) shows the deflection velocity for the thick and thin concrete at the same point divided by the impact velocity.

full-scale design critical breaking waves: 10, 16 and 24 m/s. For the thick shell the deflection is largest during the first half period of oscillation. For the thin shell the later deflection peaks are of similar magnitude as the first. Plot (c) and (d) shows the shell deflection velocity near its centre (at pt 2–2) divided by the impact velocity V for the thick, and for the thin shell respectively. The horisontal axis shows the time divided by the dry natural period of the governing mode, mode 2 (ref. Fig. 23). The thick concrete shell is accelerated to a velocity of 0.39 V during the time before the first negative deflection peak for the impact velocity of 16 m/s. The same value is about 0.53 V for the thin shell. The shell deflects inward and then outward and consistently reaches higher deflection speed on the way outward for both shells. The plot shows that the deflection velocity is considerably larger for the thin shell than the thick shell. Faltinsen (1997), studied the impact of a flat, horizontal beam impacting a flat free surface with zero deadrise angle. In that case the averaged deflection velocity was equal the impact velocity initially. Since the beam was fixed at both ends, it meant that the deflection velocity in the middle of the beam was larger than the impact velocity. In the present case however, the concrete shells do not reach a deflection velocity which is equal to the impact velocity in an averaged sense. A second difference between the beam in Faltinsen (1997) and the concrete shells is that the centre point deflection velocity is much larger, O(40%), when the shell deflect back outwards than during the initial inward deflection.

The key question is to what extent the structural vibration modifies the hydrodynamic load. If such load modification did not occur, then the response would be obtained through an ordinary dynamic analysis with slamming pressures valid for a rigid cylinder. To answer this question the hydrodynamic load terms in Eq. (19) which depends on the structural vibration are studied. These terms are the time dependent added mass force $-[A]\{\ddot{Z}\}$ and the force $-[\dot{A}]\{\dot{Z}\}$. The

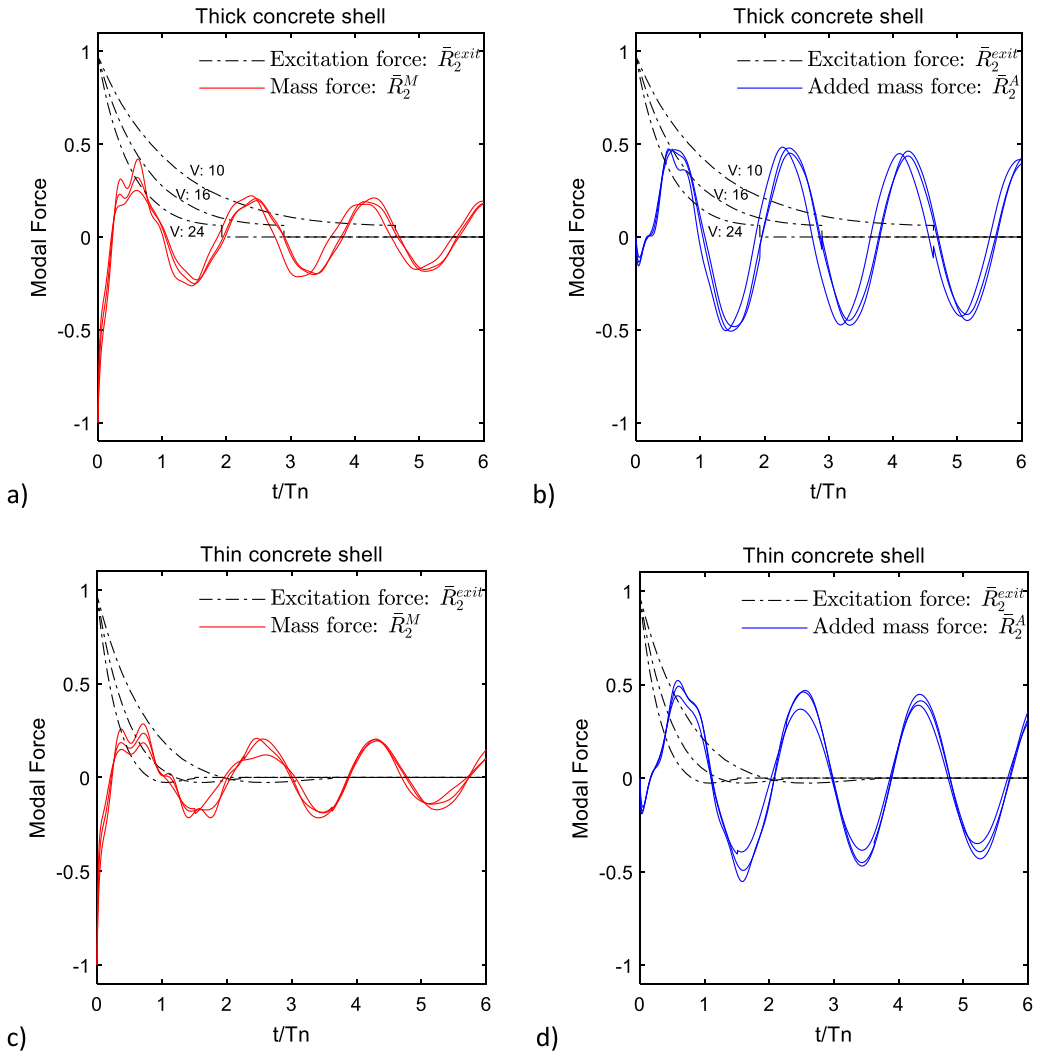

Fig. 26. Structural and added mass modal force for the equilibrium equation of the governing mode compared with the corresponding excitation (slamming) force. Plot (a) shows the structural mass force and plot (b) with the added mass force for the thick full-scale concrete shells. Plot (c) and plot (d) shows similar plots for the thin full-scale concrete shells. (For interpretation of the references to colour in this figure legend, the reader is referred to the web version of this article.)

force term from the transient added mass of the governing mode is studied in detail and compared with the excitation (slamming) force of the same mode. The plots in Fig. 26 show the nondimensional excitation force for mode 2, $-\dot{A}_{20}(t)V$, divided by its initial (extreme) value $F_2^{exit} = -\dot{A}_{20}(t = 0)V$. This force is denoted $\bar{R}_2{}^{exit}$ and is plotted for all plots for reference. There is one dotted black curve for each of the three impact velocities; 10, 16 and 24 m/s. Plots (a) and (c) shows the modal mass force of the second mode $\bar{R}_2^M = -M_{22}\ddot{Z}_2/F_2^{exit}$ for the same impact velocities as red curves. Plots (b) and (d) shows the hydrodynamic modal added mass force for the same mode, $\bar{R}_2^A = -[A_{2:}]\{\ddot{Z}\}/F_2^{exit}$. Here, $[A_{2:}]$ is the second row of the matrix $[A]$. Comparing the modal structural mass force for the thick concrete shell, plot (a) with the modal added mass force for the same shell, the two curves differ initially. The structural mass force starts at -1, perfectly balancing the excitation force at this moment, the modal added mass force starts at zero, and does not contribute significantly to balance the modal excitation force initially. Later in the impact when the shell is deflecting inward for the first time at ~0.6 t/Tn, the added mass force is a bit higher than the structural mass.

The matrix equation Eq. (19) has a term $[\dot{A}]\{\dot{Z}\}$ which is proportional both the impact velocity and the deflection velocity. This term is by no means new and is contained in previous research works like for instance (Ionina and Korobkin, 1999; Faltinsen, 1999, 1997). However, its relative importance has not been adequately addressed. Here the term $[\dot{A}]\{\dot{Z}\}$ is denoted the slam damping since it is linked to the slamming force and that it is proportional to the deflection velocity. The nondimensional version of the slam damping term is written as $\bar{R}_2^{SD} = -[\dot{A}_{2:}]\{\dot{Z}\}/F_2^{exit}$ and is plotted in Fig. 27. $[\dot{A}_{2:}]$

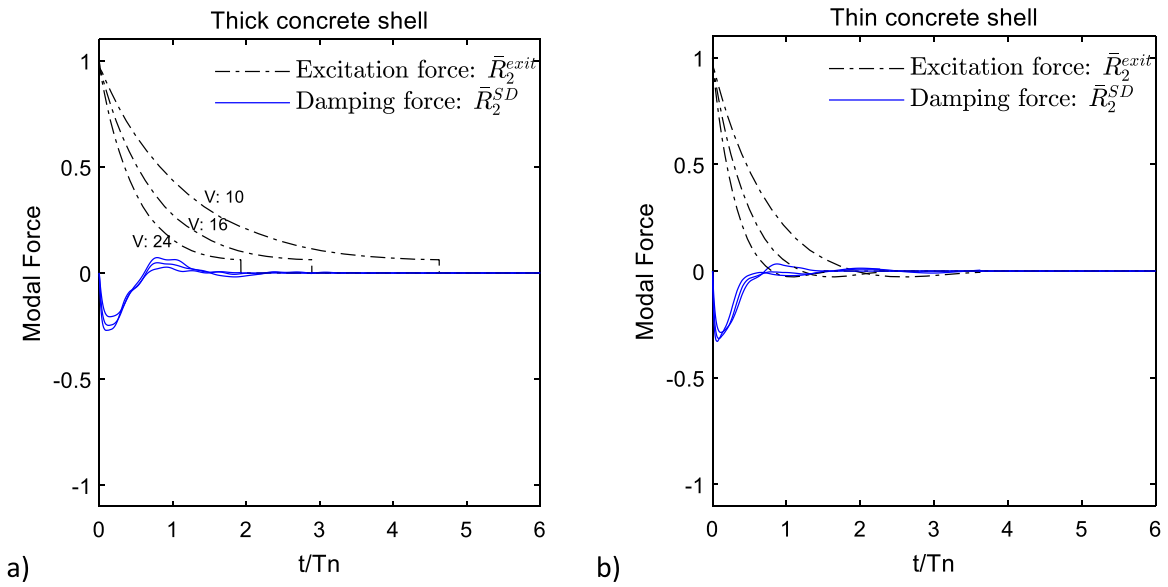

Fig. 27. The plots show the time series of the nondimensional hydrodynamic slam damping term compared with the excitation (slamming) force for (a) the thick concrete shell and (b) the thin concrete shell.

refers to the second row of the matrix $[\dot{A}]$. plot (a) of Fig. 27 shows this force for the thick concrete shell and plot (b) shows this force for the thin concrete shell. This hydrodynamic force term acts in the opposite direction of the excitation force. Its significant contribution lasts only until the maximum deflection of the shell at about 0.6 t/Tn. The plots show that the slam damping force acts with significant magnitude in the opposite direction of the slamming force. Furthermore, the plots show that this load term is more important for the thin concrete shell than for the thick concrete shell. Considering the impulse of this hydrodynamic slamming damping term compared to the impulse of the excitation force, it is evident that the importance of this term increases with impact velocity.

The effect of hydroelasticity can be defined as the modification of the hydrodynamic pressure due to the structural response. But which of the two hydroelastic terms are most important: added mass or slam damping? To answer this question, a set of numerical simulations is carried out systematically by removing terms in Eq. (19): First an hydroelastic analysis including all terms, then an analysis neglecting slam damping, then an analysis neglecting added mass and finally an analysis neglecting both added mass and slam damping.

Fig. 28 shows the time series of hoop bending moment close to the shell centre (pt. 4) divided by the extreme static hoop bending moment at the same location for the thick (a) and the thin (b) concrete shells both for an impact velocity of 24 m/s. The blue curve shows the hydroelastic solution according to Eq. (19). The added mass term modifies the period of vibration but does not modify the extreme bending moment significantly (blue dashed line compared to blue full line, red dashed line compared to red full line). The slam damping term cause significant reduction of the extreme bending moment but does not modify the period of vibration significantly (blue full lines compared to red full lines, blue dashed lines compared to red dashed lines). Fig. 28(c) and (d) shows the corresponding nondimensional hoop membrane force close to the shell centre. Here the importance of the slam damping term is similar as for the hoop bending moment. However, the effect of added mass is much larger on the extreme membrane force than on the extreme bending moments. Including added mass means increasing the hoop membrane force.

In the following text, the effect of the added mass and slam damping on the extreme responses are investigated for a whole range of impact velocities.

Fig. 29(a) and (b) shows the extreme bending moment close to the centre point (pt. 4) as a function of impact velocity for the thick and thin concrete shells. The plot shows that the slam damping term is important for estimating correct extreme bending moment and that the inclusion of this term in the analysis reduces the extreme hoop bending moments. Whether or not added mass is included has limited effect when considering bending moments.

Fig. 29(c) and (d) show the extreme hoop membrane forces close to the centre point (pt. 4). Again, inclusion of the slam damping term reduces the calculated extremes. Added mass is more important for extreme hoop membrane forces than extreme hoop bending moments. However, inclusion of added mass increases the extreme hoop membrane force while inclusion of slam damping reduces it. These findings are not sensitive to large variations of the impact velocity.

10. Discussion

The presented study shows how concrete shells respond to violent slamming on a calm water surface. The two shells in the study represent reinforced and prestressed concrete shells with a diameter of 31 m, with a height of 24.6 m, and

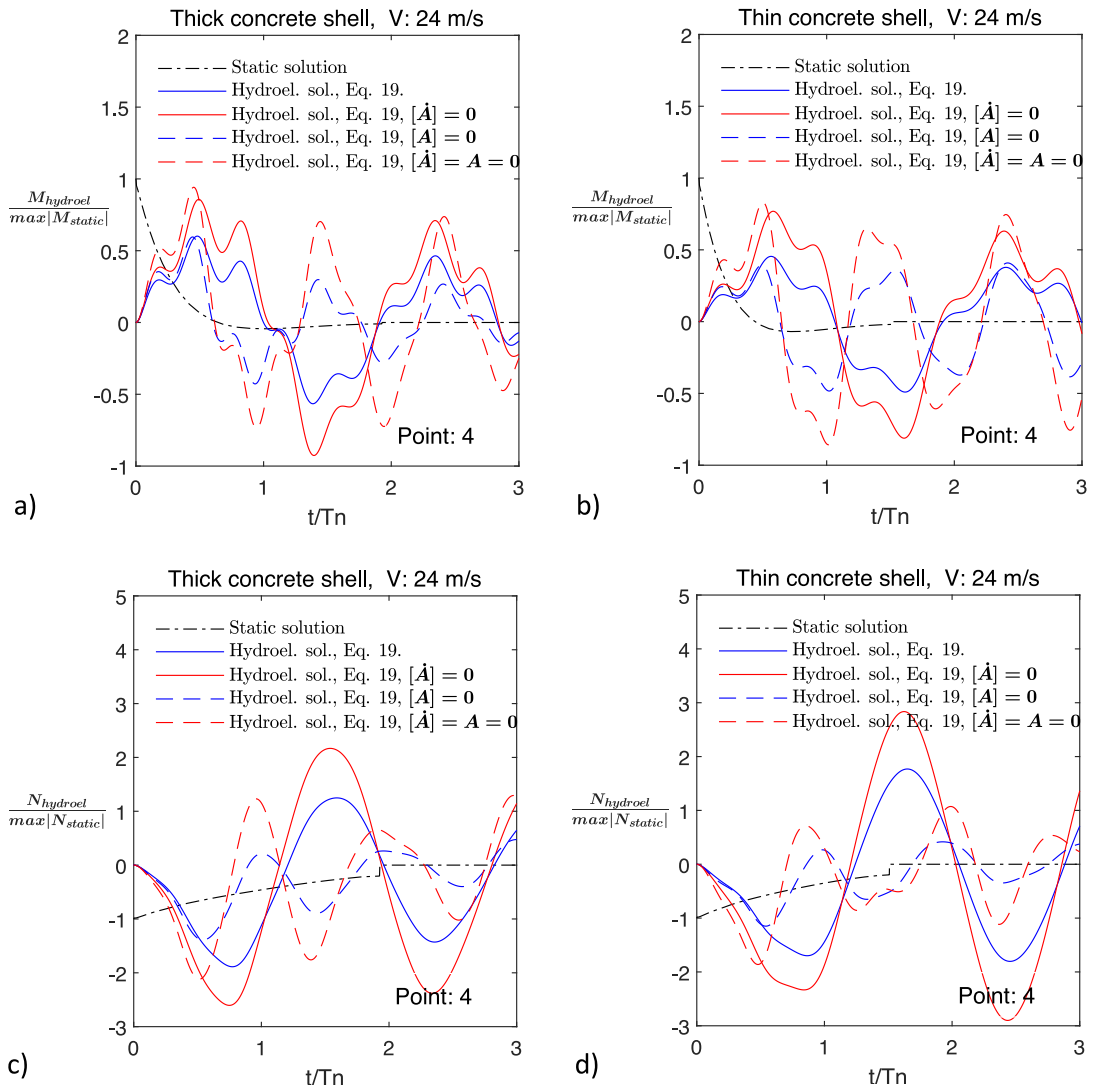

Fig. 28. Plots showing the effect of added mass and slam damping on nondimensional hoop bending moments at the shell centre (pt. 4). For the thin (a) and thick (b) concrete shell. Plot (c) and (d) shows corresponding plots for the hoop membrane force at the same location. (For interpretation of the references to colour in this figure legend, the reader is referred to the web version of this article.)

covering 77.3 degrees of the circular cylinder. The thick shell represents a full-scale thickness of 872 mm while the thin shell represents a thickness of 584 mm. The water impact tests are carried out with Froude scaled elastic model shells at a geometrical scale of 1:55.

The slamming pressures are carried by a combination of shell membrane forces, bending moments and structural mass forces. The proper Froude scaling principles for the material properties were derived and showed that the model shell should satisfy the following five conditions: $E = \check{r}\lambda\overline{E}$, $h = \lambda\overline{h}$, $\rho_c h = \check{r}\lambda\overline{\rho}_c\overline{h}$, $\nu = \overline{\nu}$, $\rho = \check{r}\overline{\rho}$ for geometric scaling factor λ, Young's modulus E, shell thickness h, shell mass density ρ_c, Poisson ratio ν and water density ratio between full sand model scale, $\check{r}$. Barred quantities are properties in model scale. These conditions are quite restrictive, and a relevant material is hard to identify for such a small scale (1:55). A simplified approach is adopted where scaling of the bending stiffness and the mass per area are given priority and are scaled according to $D = \overline{D}\check{r}\lambda^4$ and $m = \overline{m}\check{r}\lambda$. Polycarbonate, which is a reliable material with low Young's modulus, was selected for the Froude scaled elastic model shells to minimize the shell scaling errors as much as possible.

A hydroelastic method was presented, formulating the deformation of the shell in terms of dry natural modes calculated using finite element shell analysis. The hydrodynamic boundary value problem was solved for different wetted areas of the cylinder, using 2D strip theory with 3D corrections and the flat plate approximation. Furthermore, the velocity potential was set to zero on the free surface. In the calculation of the wetted area of the cylinder the deformation of the shell was neglected.

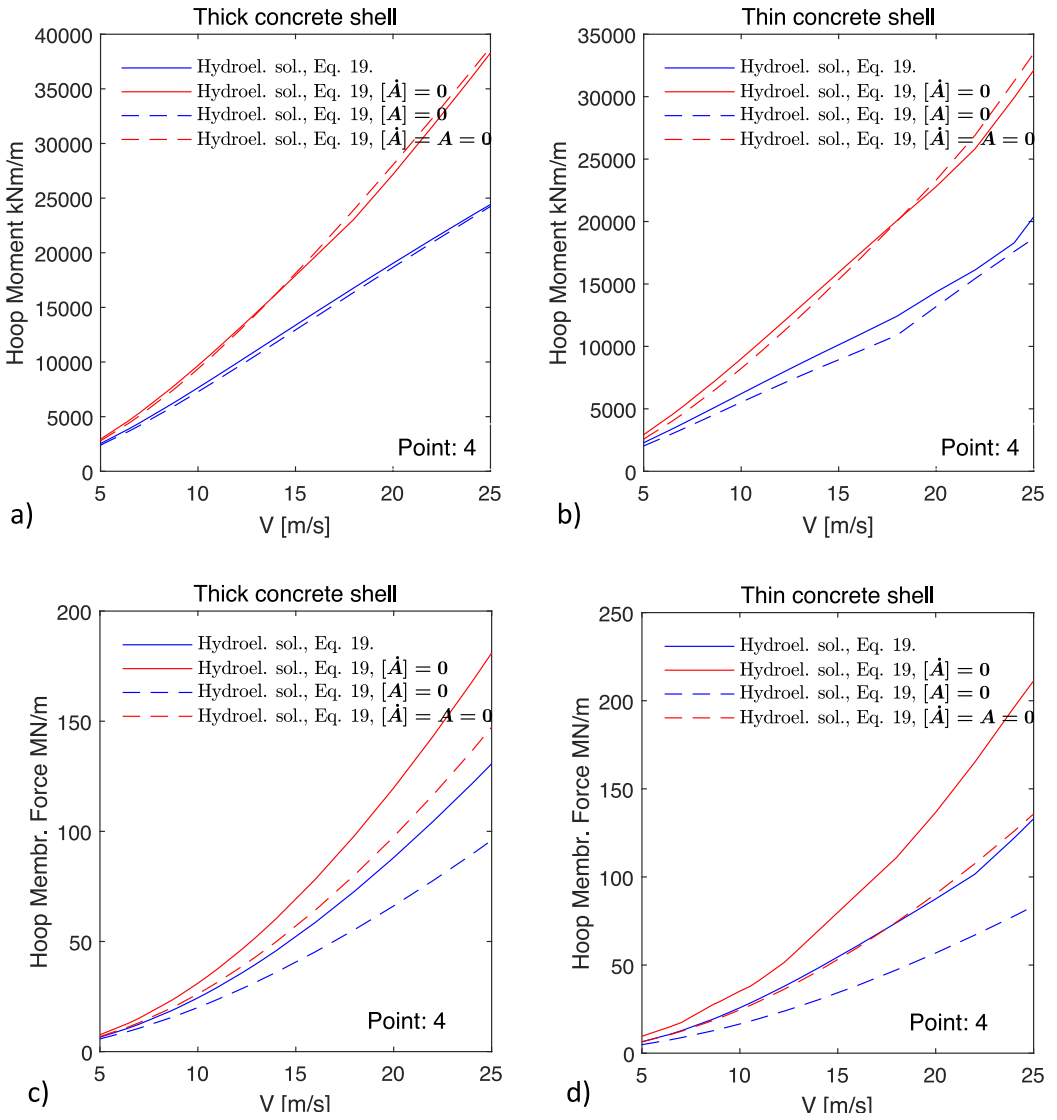

Fig. 29. Extreme hoop bending moment (a) and hoop membrane force (b) close to shell centre as a function of impact velocity V. The plot express how added mass and slam damping affect the extreme responses of the shell.

The deviation between calculated and measured extreme hoop bending moments and membrane forces were calculated and compared for the thick and the thin elastic shells. This difference was calculated as the mean deviation for all the four drop heights tested. The most significant difference was the overprediction of the bending moments for the thick elastic shell. For measurement point 1 to 5 the bending moments were systematically overestimated by ∼20%. The uncertainties of the strain gauges and Young's modulus of the polycarbonate material is not sufficient to explain this difference. Probable unknown causes of this difference may exist in the experimental set up or inaccuracies of the hydroelastic method. The mean deviation was far less for the extreme hoop membrane force for points 1 to 5 for the thick shell. Measurement point 6 on the thick elastic section is likely defect since the measured bending moments and membrane forces were much lower than at point 1 on the same elastic shell. Although point 1 and 6 are not located completely symmetrically, the strains are not expected to be that different. This is supported by the measurements on the thin elastic section and the hydroelastic calculations for both the thin and the thick elastic shells. A physical cause of this defect was not identified. For the thin elastic shell, the mean deviation of the bending moments were more accurate than for the thick shell, i.e. between −22% to 15% for all measurement points. The corresponding mean deviation for the extreme membrane force for the thin elastic shell were between −15% and 16%. It is concluded that the hydroelastic method although simplified, compares well with measurements. Furthermore, the hydroelastic method provide quite accurate estimates and captures the most important physics of the impact.

The accuracy of the Froude scaled elastic model shells were quantified through comparisons of simulation results for the full-scale concrete shells and for the Froude scaled elastic shells. Both the hoop bending moments and the hoop membrane force are larger for the Froude scaled elastic shells than for the full-scale concrete shells. The latter is true for all measurement points, both thin and thick concrete shell. The scaling error for the extreme hoop bending moment near the shell centre ranges from 8% and 33% for both concrete shells. For the hoop membrane force scaling error is significantly less (in the range from 2% to 16%). The shell scaling error increase with the impact velocity. The estimated errors above (%) are calculated for 10 and 25 m/s respectively.

11. Conclusion

This research shows how realistic Froude scaled elastic shells representing concrete shells can be designed. Furthermore, the results show that even large, thick and heavy concrete shells experience significant hydroelastic effects during slamming.

The effect of hydroelasticity was studied through (1) dynamic amplification DAF and (2) hydrodynamic load modifications due to structural vibration. DAFs were derived for the most loaded measurement points near the centre of the shell. For typical design-critical 100- and 10.000-year wave slamming events impact velocities in the range 10–24 m/s. For this range of impact velocities relevant DAFs were calculated: The lowest DAFs are seen for the hoop bending moment for both the thin and the thick shells ranging from 0.5 to 1.13. Then follows the displacement ranging from 0.73 to 1.38 and the hoop membrane force ranging from 1.8 to 2.18. Hence, the magnitude of the DAF strongly depends on which response which is considered.

The time series from experiments and numerical calculations shows one governing frequency of response. Furthermore, the numerical method shows that two modes are main contributors to the response. The governing mode has three half waves in the hoop direction of the shell while one half wave in the axial direction. This mode governs the deflection, bending moment and membrane force at all measurement points. The secondary mode has two half waves in the hoop direction while one half wave in the axial direction. This mode contributes to the deflection on the sides of the shell and the membrane force at all locations on the shell.

The centre point deflection velocity time history of the full-scale concrete shells showed oscillations dominated by one frequency but with modulations due to higher frequency components. Interestingly, the centre point deflection velocity during the time of the initial inward deflection was much less than the impact speed. For an impact speed of 16 m/s the centre point inward deflection velocity was equal to 39% and 53% of the impact velocity for the thin and the thick concrete shell respectively. The shells deflected inward and then outward at the centre of the shell, consistently reaching higher deflection velocity on the way outward for both concrete shells.

The modification of the hydrodynamical load due to structural vibrations was investigated. The hydroelastic numerical method was used to isolate the individual contributions. The first observation is that slamming force at the initial moment of impact is balanced by structural mass alone. The second observation is that the added mass force has a rapid rise-time and reaches the same order of magnitude as the structural mass force by the time of maximum response of the shell at $0.6T_n$. Here T_n is the dry natural frequency of the governing mode of response. After this time instant the added mass and structural mass behaves similarly for the governing mode. The third observation is the *slam damping* term. This term is proportional to both the impact velocity and the deflection velocity. This force is significant from the initial moment of impact and until the time of maximum response, $t = 0.6T_n$ for both shells. After this the term is negligible.

The relative importance of the added mass and slam damping terms were investigated by systematically turning the added mass and slam damping terms on and off. These simulations show that the effect of including slam damping reduces the hoop bending moment by 21% and 35% for the thick shell and 31 and 39% for the thin shell, for impact velocities of 10 and 24 m/s, respectively. The effect of including slam damping reduce the estimated hoop membrane force with a similar amount. On the contrary, the effect of including added mass is small considering extreme hoop bending moments but is seen to significantly increase the estimated extreme hoop membrane forces.

Generally, structural responses are seen to significantly modify the hydrodynamic loads during impact. These load modifications should be properly accounted for when designing concrete shells exposed to slamming.

CRediT authorship contribution statement

Bjørn C. Abrahamsen: Supervision, Conceptualization, Resources, Methodology, Software, Validation, Formal analysis, Investigation, Resources, Writing – original draft, Writing – review & editing, Visualization. **Frode Grytten:** Supervision, Conceptualization, Resources. **Øyvind Hellan:** Supervision, Conceptualization, Writing – review & editing. **Tore H. Søreide:** Supervision, Conceptualization, Methodology. **Odd M. Faltinsen:** Supervision, Conceptualization, Methodology, Writing – review & editing.

Declaration of competing interest

The authors declare that they have no known competing financial interests or personal relationships that could have appeared to influence the work reported in this paper.

Data availability

Data will be made available on request.

Acknowledgements

This study was supported by Equinor, Norway, Aker Solutions, Norway, Multiconsult, Norway, the Norwegian Shipowners Association and the Research council of Norway (RCN) through the SLADE KPN project (RCN Project No. 294748). One of the co-authors is connected with the Centre of Excellence AMOS, supported by RCN, Norway through the Centres of Excellence funding scheme AMOS, (RCN project No. 223254).

References

Abrahamsen, B.C., 2011. Sloshing Induced Tank-Roof Impact with Entrapped Air Pocket (Ph. D. thesis). Norwegian university of Science and Technology, NTNU.
Abrahamsen, B.C., Alsos, H.S., Aune, V., Fagerholt, E., Faltinsen, O.M., Hellan, Ø., 2020. Hydroplastic response of a square plate due to impact on calm water. Phys. Fluids 32, 082103.
Arai, M., Miyauchi, T., 1998. Numerical study of the impact of water on cylindrical shells, considering fluid structure interactions. In: PRADS'98. Hague.
Cao, K., Wang, Y., Wang, Y., 2012. Effects of strain rate and temperature on the tension behaviour of polycarbonate. Mater. Des. 38, 53–58.
Cao, Kan, Wang, Yang, Wang, Yu, 2014. Experimental investigation and modeling of the tension behavior of polycarbonate with temperature effects from low to high strain rates. Int. J. Solids Struct. 51, 2539–2548.
Clough, R.W., Penzien, J., 1975. Dynamics of Structures. McGraw-Hill.
Cook, R.D., Malkus, D.S., Plesha, M.E., Witt, R.J., 2002. Concepts and Applications of Finite Element Analysis, fourth ed. John Wiley & Sons.
DNV, 2019. Horizontal Wave Impact Loads for Column Stabilised Units. Det Norske Veritas. Offshore technical guidance. DNVGL–OTG–14.
Faltinsen, O.M., 1997. The effect of hydroelasticity on slamming. Phil. Trans. R. Soc. London. A 355, 575–591.
Faltinsen, O.M., 1999. Water entry of a wedge by hydroelastic orthotropic plate theory. J. Ship Res. 43, 180–193.
Faltinsen, O.M., 2006. Hydrodynamics of High-Speed Marine Vehicles. Cambridge University Press.
Faltinsen, O.M., Timokha, A.N., 2009. Sloshing. Cambridge University Press.
FIB, 2010. Model code for concrete structures. fédération internationale du béton.
Ionina, M.F., Korobkin, A.A., 1999. Water impact on cylindrical shells. In: 14th International Workshop on Water Waves and Floating Bodies. USA.
ISO, 2019. ISO 527-1 plastics, determination of tensile properties. International Organization for Standardization.
Leissa, A.W., 1973. Vibration of Shells. NASA SP-288, (available online).
Meyerhoff, W.K., 1970. Added masses of thin rectangular plates calculated from potential theory. J. Ship Res. 14, 100–110.
Næss, A., Moan, T., 2012. Stochastic dynamics of marine structures.
Nastran, M.S.C., 2019. Feature pack 1, finite element analysis software.
NS3473, 2003. Concrete structures - design and detailing rules. standard norge.
Shibue, T., Ito, Ä., Nakayama, E., 1994. Structural response analysis of cylinders under water impact. In: Hydroelasticity in Marine Technology, Vol. May. Trondheim, pp. 221–228.
Sun, H., Faltinsen, O.M., 2006. Water impact of horizontal circular cylinders and cylindrical shells. Appl. Ocean Res. 28, 299–311.
Timoshenko, S.P., Woinowsky-Krieger, S.S., 1959. Theory of Plates and Shells, second ed McGraw Hill, New York.
Wåsjø, K., Stavang, T.P., Søreide, T.H., 2017. Concrete Modelling for Extreme Wave Slam Events. In: Proceedings of the ASME 2017 36th International conference on Ocean, Offshore and Arctic Engineering. OMAE 2017-61331. Trondheim, Norway.
Wagner, H., 1932. Uber stoss- und gleitvorgange an der oberflache von flussigkeite. Z. Angew. Math. Mech. 12 (4), 193–215.
Wamit, 2020. WAMIT user manual (www.wamit.com).